Evolution of structure and shapes in ^{158}Er to ultrahigh spin

J. Simpson,[1,*] M. A. Riley,[2] A. Pipidis,[2] E. S. Paul,[3] X. Wang,[2,†] P. J. Nolan,[3] J. F. Sharpey-Schafer,[4] A. Aguilar,[2,‡] D. E. Appelbe,[1] A. D. Ayangeakaa,[5] A. J. Boston,[3] H. C. Boston,[3] D. B. Campbell,[2,‡] M. P. Carpenter,[6] C. J. Chiara,[6,7,8,§] P. T. W. Choy,[3] R. M. Clark,[9] M. Cromaz,[9] A. O. Evans,[3] P. Fallon,[9] U. Garg,[5] A. Görgen,[9,‖] D. J. Hartley,[10] R. V. F. Janssens,[11,12] D. T. Joss,[1,¶] D. S. Judson,[3] F. G. Kondev,[6] T. Lauritsen,[6] I. Y. Lee,[9] A. O. Macchiavelli,[9] J. T. Matta,[5,**] J. Ollier,[1,††] M. Petri,[9,‡‡] J. P. Revill,[3,§§] L. L. Riedinger,[13] S. V. Rigby,[3] C. Teal,[2,‖‖] P. J. Twin,[3] C. Unsworth,[3,¶¶] D. Ward,[9] S. Zhu,[6,a] and I. Ragnarsson[14]

[1]*STFC Daresbury Laboratory, Daresbury, Warrington WA4 4AD, United Kingdom*
[2]*Department of Physics, Florida State University, Tallahassee, Florida 32306, USA*
[3]*Department of Physics, University of Liverpool, Liverpool L69 7ZE, United Kingdom*
[4]*Department of Physics, University of Zululand, P/B X1001, KwaDlangezwa, 3886, South Africa*
[5]*Department of Physics, University of Notre Dame, Notre Dame, Indiana 46556, USA*
[6]*Physics Division, Argonne National Laboratory, Argonne, Illinois 60439, USA*
[7]*Nuclear Engineering Division, Argonne National Laboratory, Argonne, Illinois 60439, USA*
[8]*Department of Chemistry and Biochemistry, University of Maryland, College Park, Maryland 20742, USA*
[9]*Nuclear Science Division, Lawrence Berkeley National Laboratory, Berkeley, California 94720, USA*
[10]*Department of Physics, U.S. Naval Academy, Annapolis, Maryland 21402, USA*
[11]*Department of Physics and Astronomy, University of North Carolina, Chapel Hill, North Carolina 27599, USA*
[12]*Triangle Universities Nuclear Laboratory, Duke University, Durham, North Carolina 27708, USA*
[13]*Department of Physics and Astronomy, University of Tennessee, Knoxville, Tennessee 37996, USA*
[14]*Division of Mathematical Physics, LTH, Lund University, P.O. Box 118, SE-221 00 Lund, Sweden*

(Received 12 December 2022; accepted 6 April 2023; published 10 May 2023)

The level structure of ^{158}Er has been studied using the Gammasphere spectrometer via the ^{114}Cd(^{48}Ca, $4n$) reaction at 215 MeV with both thin (self-supporting) and thick (backed) targets. The level scheme has been considerably extended with more than 200 new transitions and six new rotational structures, including two strongly coupled high-K bands. Configuration assignments for the new structures are based on their observed alignments, $B(M1)/B(E2)$ ratios of reduced transition probabilities, excitation energies, and comparisons with neighboring nuclei and theoretical calculations. With increasing angular momentum, this nucleus exhibits Coriolis-induced alignments of both neutrons and protons before it then undergoes a rotation-induced transition from near-prolate collective rotation to a noncollective oblate configuration. This transition occurs via the mechanism of band termination around spin $45\hbar$ in three rotational structures. Two distinct lifetime branches, consistent with the crossing of a collective "fast" rotational structure by an energetically favored "slow" terminating sequence, are confirmed for the positive-parity states, and similar behavior is established in the negative-parity states. Weak-intensity, high-energy transitions are observed to feed into the terminating states. At the highest spins,

[*]john.simpson@stfc.ac.uk
[†]Present address: Department of Physics, California Polytechnic State University, San Luis Obispo, California 93407, USA.
[‡]Present address: Lawrence Livermore National Laboratory, 7000 East Ave., Livermore, California 94550-9234, USA.
[§]Present address: DEVCOM Army Research Laboratory, Adelphi, Maryland 20783, USA.
[‖]Present address: Department of Physics, University of Oslo, N-0316 Oslo, Norway.
[¶]Present address: Department of Physics, University of Liverpool, Liverpool L697ZE, United Kingdom.
[**]Present address: Physics Division, Oak Ridge National Laboratory, Oak Ridge, Tennessee 37830, USA.
[††]Present address: Rapiscan Systems, Prospect Way, Victoria Business Park, Biddulph, Stoke-on-Trent ST8 7PL, United Kingdom.
[‡‡]Present address: School of Physics, Engineering and Technology, University of York, Heslington, York YO10 5DD, United Kingdom.
[§§]Present address: Radiometric Systems Group, Sellafield Ltd, Seascale CA20 1PG, United Kingdom.
[‖‖]Present address: Nuclear Regulatory Commission, T4L7 11555 Rockville Pike, Rockville, Maryland 20855, USA.
[¶¶]Present address: STFC Daresbury Laboratory, Daresbury, Warrington WA44AD, United Kingdom.
[a]Deceased.

three collective bands with high dynamic moments of inertia and large quadrupole moments were identified. These bands are interpreted as triaxial strongly deformed structures and mark a return to collectivity at ultrahigh spin.

DOI: 10.1103/PhysRevC.107.054305

I. INTRODUCTION

Heavy rare-earth nuclei around mass 160 are predicted to accommodate the highest values of angular momentum, or spin, prior to fission [1], and hence this region of the nuclear chart has traditionally been one of the most favored domains for studying high-spin discrete energy levels in the atomic nucleus [2]. The excitement generated by many fascinating discoveries in this region has played a major role in advancing the development of more sensitive γ-ray detector systems. The discoveries in ^{158}Er have benefited greatly from the evolution of detector systems through the decades. As a result, the nucleus ^{158}Er has been used as a classic example in many textbooks, for example Refs. [3–11], due to the variety of phenomena that occur with increasing angular momentum and excitation energy. In addition, several review articles have featured ^{158}Er, the most recent being Ref. [12]. This evolution of structure with spin in ^{158}Er is illustrated in Fig. 1.

As the angular momentum increases, this nucleus exhibits Coriolis-induced alignments of both neutron and proton pairs along the yrast line (see Fig. 2 for a sample spectrum and an alignment plot). It was among the first examples in which backbending was discovered [16,17] ($I \approx 14$), and was the first nucleus where the second ($I \approx 28$) and third ($I \approx 38$) discontinuities along the yrast line were identified [18,19]. At spins 40–50 $\hbar$ the yrast line is crossed by a very different structure, where the ^{158}Er nucleus undergoes a dramatic transition from near-prolate collective rotation to noncollective oblate configurations [20–24]. This transition ultimately leads to favored, fully aligned band-termination configurations [25–27]. In ^{158}Er, three such terminating states have been observed at $I^{\pi} = 46^{+}$, 48^{-}, and 49^{-} [23]. Band termination reveals the underlying finite-particle basis of nuclear angular-momentum generation [7,8].

It took several decades, and more sensitive detector systems, to reveal the structures at higher spin beyond band termination in ^{158}Er. The first was the identification of high-energy transitions populating the terminating states. These were established in ^{157}Er [28,29] in the same experiments reported here, and interpreted as $Z = 64$ core breaking excitations. Similar transitions feeding the terminating states in ^{158}Er were initially reported in Ref. [24,30]. These transitions only increased the observed spin up by $1\hbar$ or $2\hbar$. The major advance in pushing to the highest spins was the observation of two rotational structures in ^{158}Er (as well as two in ^{157}Er), with high dynamic moments of inertia that extended up to spin $\approx 65\hbar$ bypassing the band terminating states [15,30], marking a dramatic return to collectivity. The complementary thick-target experiment confirmed that these collective bands possess large transition quadrupole moments [31]. They have been interpreted as triaxial strongly deformed (TSD) structures based on a comparison of transition quadrupole moments (Q_t) between experiment and theory [31], and long standing predictions that such heavy nuclei will possess nonaxial shapes on their path towards fission [25,26]. A third band with similar character was subsequently discovered [32].

A comprehensive level scheme of ^{158}Er with six new rotational structures, including two strongly coupled high-K bands, and new excited states feeding into the band terminating states, are presented. Configuration assignments are proposed for the new structures based on their observed alignments, $B(M1)/B(E2)$ ratios, excitation energies, and comparisons with neighboring nuclei and theoretical calculations. This work complements the previous publications of ^{158}Er for the "ultrahigh-spin" TSD bands [15,31,32].

II. EXPERIMENT AND DATA ANALYSIS

High-spin structures in ^{158}Er were studied in two experiments using the Gammasphere spectrometer [33,34]. The first was performed at Lawrence Berkeley National Laboratory and the second at Argonne National Laboratory, with Gammasphere consisting of 102 and 101 escape-suppressed high-purity germanium (HPGe) detectors, respectively. In the first experiment, a 215 MeV ^{48}Ca beam was delivered by the 88-inch Cyclotron and bombarded two stacked thin self-supporting foils of ^{114}Cd, of total thickness 1.1 mg/cm^2. A total of 1.2×10^9 events were recorded, each one containing at least seven escape-suppressed coincident γ rays (fold $\geqslant$ 7). In the second experiment, a ^{48}Ca beam of the same energy was delivered by the ATLAS facility and bombarded a 1 mg/cm^2 ^{114}Cd target backed by a 13 mg/cm^2 ^{197}Au layer. A 0.07 mg/cm^2 ^{27}Al layer between the Cd and Au was used to prevent the migration of the target material into the backing. A total of 9.9×10^9 events were accumulated, each one containing at least four coincident γ rays (fold $\geqslant 4$). In the offline analyses the raw data were first sorted into a BLUE database [35], from which both cubes (three-dimensional arrays) and hypercubes (four-dimensional arrays) were created. The subsequent analyses were performed with the RADWARE software package [36,37], using its in-built background subtraction, to construct the level scheme based on γ-ray coincidence relationships and relative intensities.

One-dimensional spectra at individual detector angles were also generated directly from the BLUE database of the thin-target experiment with multiple gates set on known in-band stretched quadrupole ($E2$) transitions. Then, angle-specific spectra were analyzed to obtain angular-intensity ratios and, based on the method of directional correlations from oriented states [38–40], to determine γ-ray multipolarities. The detectors used for the angular intensity ratios were grouped into two sets, consisting of several rings in which the spectra are added together. One set contained

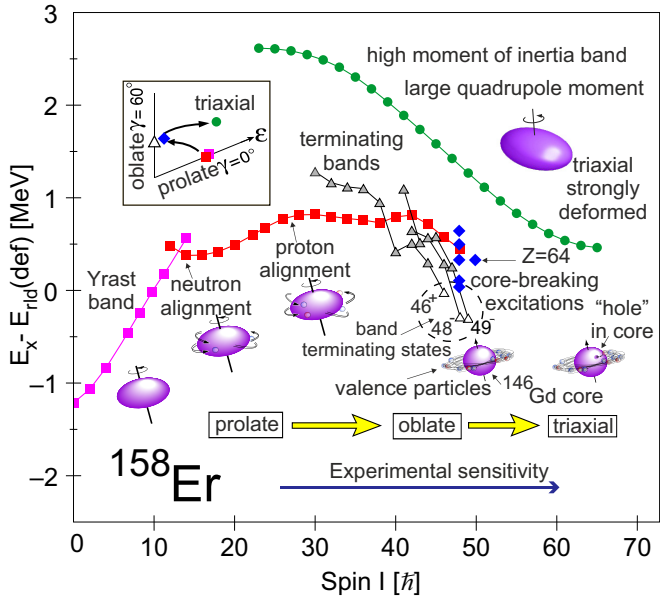

FIG. 1. The evolution of nuclear structure in ^{158}Er as a function of spin and excitation energy. The inset illustrates the changing shape of ^{158}Er with increasing spin within the standard (ε, γ) deformation plane. Excitation energies are plotted relative to a deformed rotating liquid drop reference [13]; see also [14]. This figure is adapted and updated from Ref. [15].

detectors at rings around $\theta = 35°/145°$ with respect to the beam direction, and the other set consisted of detectors at rings around $\theta = 90°$. Angular intensity ratios, R, of a transition were calculated as

$$R = \frac{I_\gamma(\theta = 35°/145°)}{I_\gamma(\theta = 90°)}. \quad (1)$$

R was normalized to 1.0 for known stretched quadrupole ($E2$) transitions. This then gives a value of ≈0.6 for a pure stretched dipole transition. Similar high-fold angular-intensity analyses have been previously published for ^{156}Er [41] and ^{157}Er [29], where the data were also obtained from the present experiments. In these latter cases, γ^4-gated spectra proved optimal for the measurements.

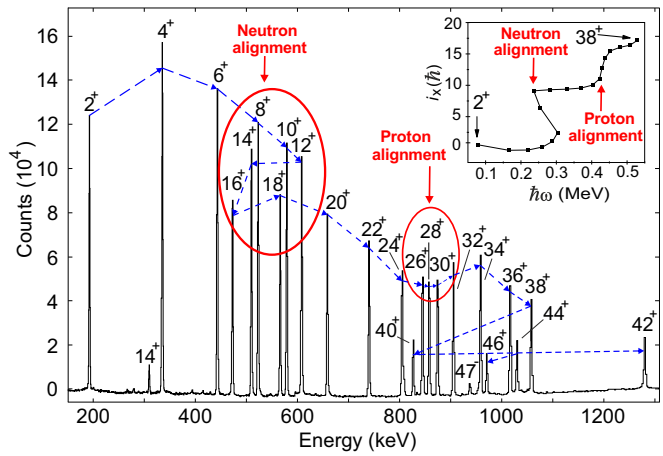

FIG. 2. Sample coincidence γ-ray spectrum from the thick target data for the yrast band in ^{158}Er. Inset: experimental alignment, i_x, as a function of the rotational frequency, $\hbar\omega$, for the yrast band. The observed neutron and proton alignments are marked in both the spectrum and the alignment plot. The dramatic change in structure towards band termination above 38^+ is evident in the spectrum.

III. RESULTS

The level scheme of ^{158}Er is presented in Figs. 3–5. Spin and parity (I^π) assignments have been either adopted from Refs. [20,23,42,43], wherever applicable, or determined based on the measured R values. If an R measurement was not possible, a tentative spin and parity assignment for a state was made based on logical assumptions, and the corresponding I^π label in the level scheme is shown in parentheses. The properties of the γ-ray transitions observed are given in the Appendix, Table IV, where they are ordered into specific bands. Overall, more than 200 transitions have been added to the level scheme, involving six new bands (bands 5, 7, 8, 9, 12, and 13), compared with previous publications. The three ultrahigh spin collective bands have been observed in ^{158}Er [15,31,32], and are included in Fig. 6. These bands have not been directly connected to the low-spin structures. However, the strongest band (TSD band 1) feeds into the yrast states at ≈25$\hbar$ and extends to ≈65$\hbar$; see Ref. [15].

A. Band 1

As shown in the partial level scheme in Fig. 3, band 1 is the ground-state band with parity and signature ($\pi = +$, $\alpha = 0$). Previous studies established this sequence up to the 28^+ level [42]. In the present work all the states up to 28^+ are confirmed, including the presence of the triplet 651, 654, and 648 keV γ rays.

The tentative $30^+ \rightarrow 28^+$ transition of 939 keV, mentioned in [42], is not seen in the present data. Rather, it has been revealed that, above the 28^+ level, band 1 splits into two distinct branches. The more energetically favored branch consists of five (tentatively six) new transitions that extend the sequence up to 38^+, possibly (40^+). The less favored branch above the 28^+ level, labeled 1a in Fig. 3, comprises three (possibly four) new transitions, which reach up to (34^+), possibly (36^+). Two new transitions, 834 and 1048 keV, are observed, connecting the two branches. Five new transitions have been observed to link band 1 with band 2, with energies of 1097, 1136, 1165, 1201, and 1270 keV.

R measurements were only possible for the transitions below the 28^+ level in band 1 and confirm the $\Delta I = 2$ ($E2$) character of these transitions (see the Appendix). Note that the R value for the lowest spin transitions are less than 1.0 due to dealignment of the spin vectors [44,45].

A coincidence γ-ray spectrum representative of this band is presented in Fig. 7. This spectrum was obtained by summing up many combinations of gates, each with the requirement that there were three transitions in the band. Gate files (lists of gates) were used to create separate coincidence gated spectra for each γ ray in the list, which were then combined to generate the final spectrum. Specifically, two lists of γ rays were created, namely a and b. List a consisted

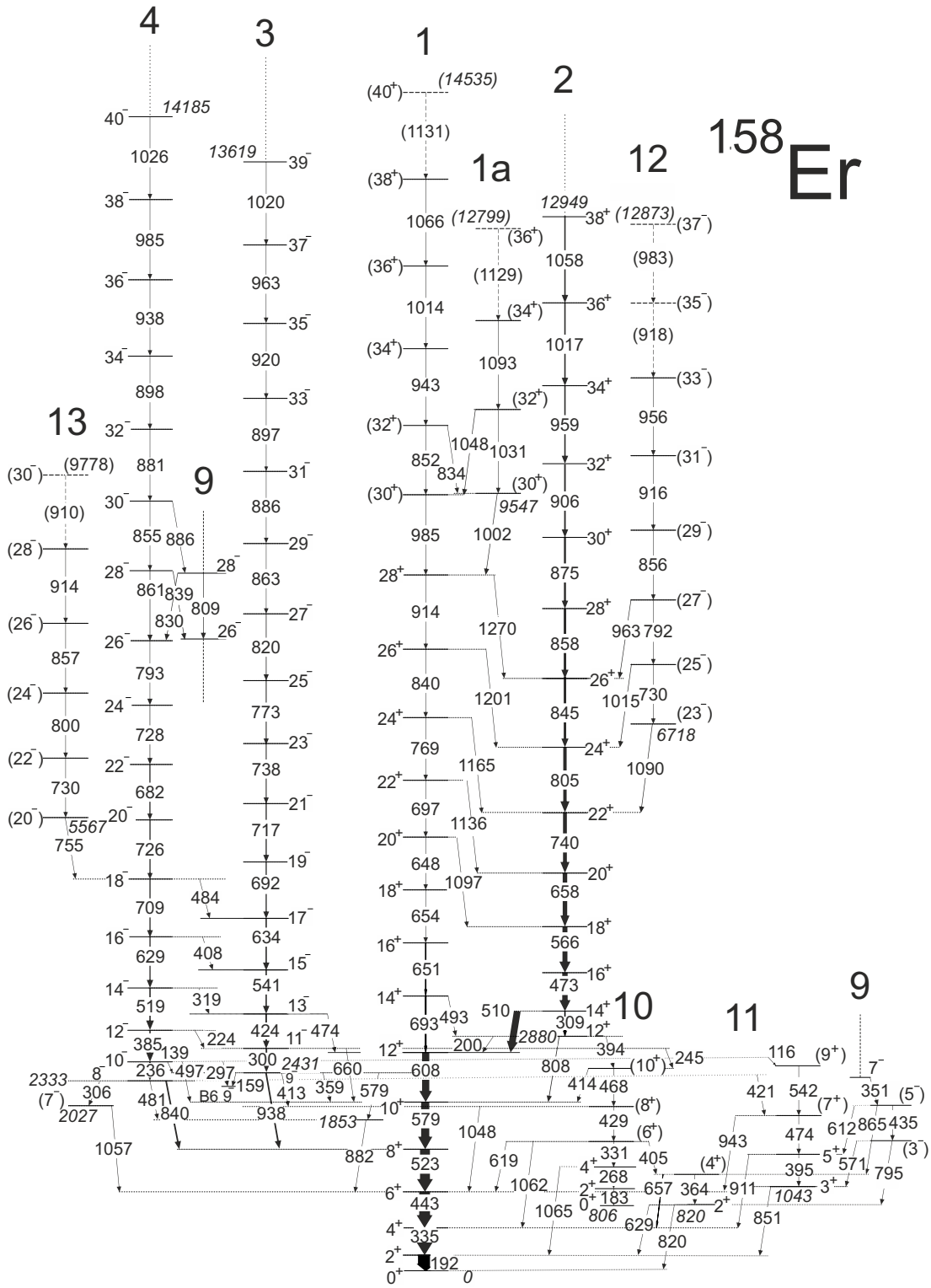

FIG. 3. Partial level scheme of ^{158}Er showing bands 1 to 4 and 10 to 13 below spin 40$\hbar$. Energies are given in keV, tentative transitions and levels are indicated by dashed lines, and tentative spins, parities, and γ-ray energies are given within parentheses. The less energetically favored branch in band 1 above 28^+ is labeled 1a. Extension of bands 2–4 to higher spin (Fig. 5) and connections to band 9 (Fig. 4) are indicated.

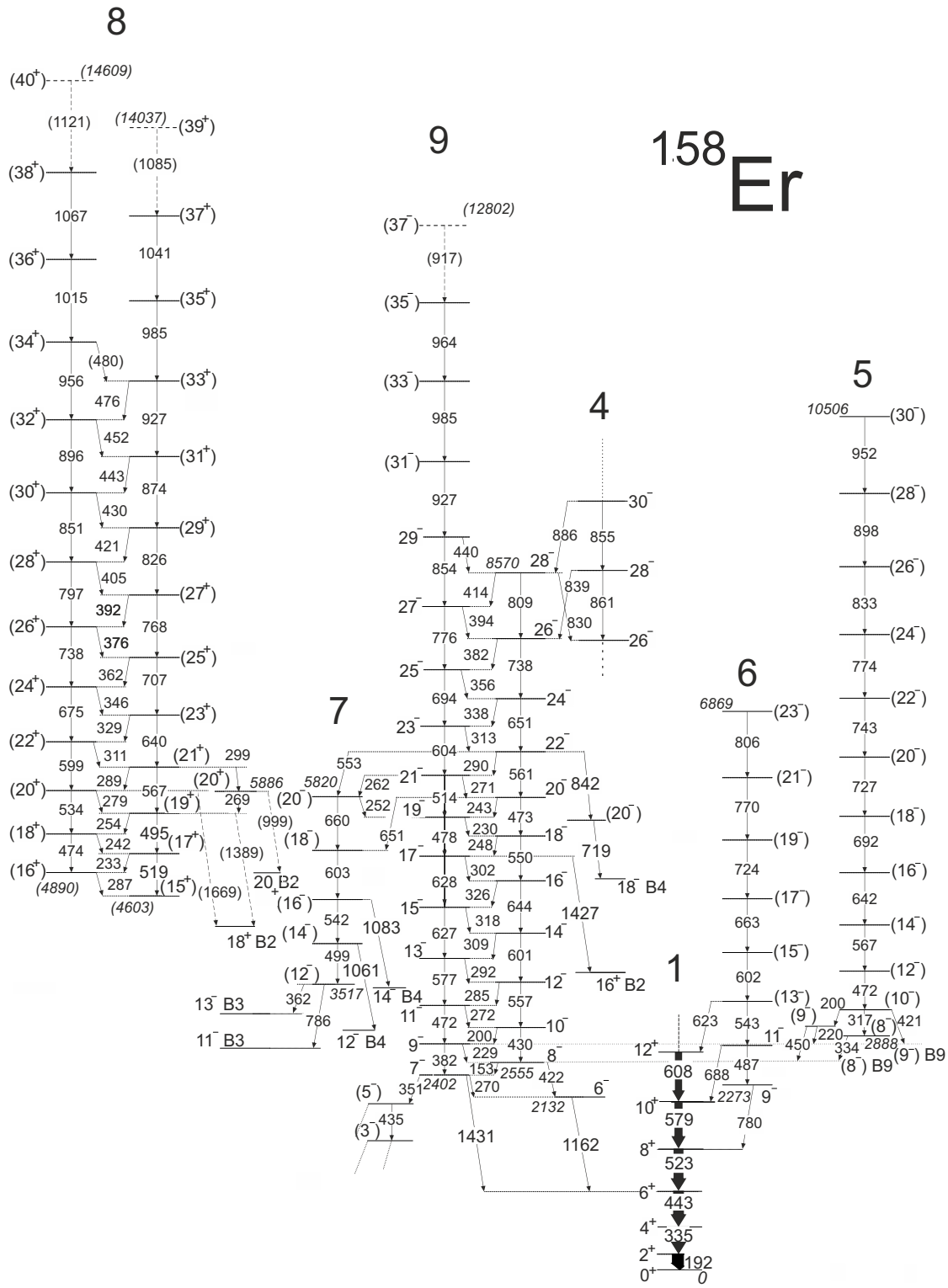

FIG. 4. Partial level scheme of ^{158}Er showing bands 5 to 9 and the low lying states in band 1. Connections to states in bands 2, 3, and 4 are indicated. The decay from band 9 via the 351 and 435 transitions are shown in Fig. 3. The same labeling convention as in Fig. 3 is employed.

of the 651, 654, 697, 769, 840, and 914 keV γ rays and list *b* included the 943, 1014, and 1066 keV γ rays. Then a triple-coincidence gate between any two (non identical) members of list *a* with one from list *b* was placed on the thick-target hypercube data.

B. Band 2

Band 2 is the yrast ($\pi = +$, $\alpha = 0$) cascade from spin 12^+ onwards (see Fig. 3). This band splits into two branches at 38^+ with the yrast states continuing to the previously

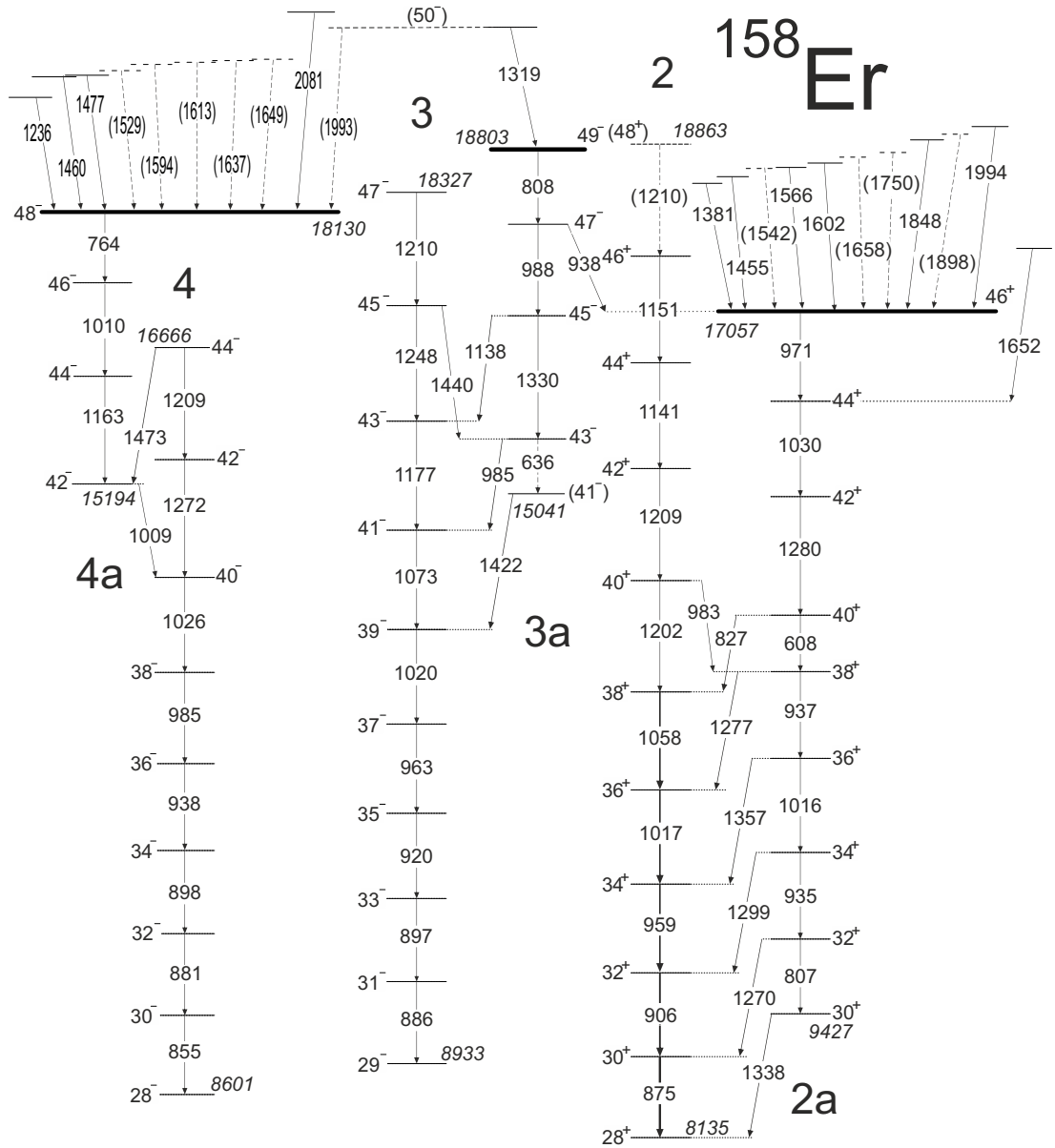

FIG. 5. High-spin section of the ^{158}Er level scheme displaying bands 2, 3, and 4 from spin 28$\hbar$. Band-terminating states at 46^+, 48^-, and 49^- are indicated by thickened lines. The same labeling convention as in Fig. 3 is employed, with additional labels, 2a, 3a, and 4a, to distinguish the terminating sequences; see discussion.

established favored terminating state at 46^+ [21,23]. This branch, labeled 2a in Fig. 5, is established from 30^+ to 46^+. In Refs. [23,24], some suggestions were made for possible transitions feeding into this special terminating state at 46^+. In the present work, five (tentatively ten) feeding transitions above the 46^+ terminating state have been identified. These feeding transitions are included in the partial level scheme in Fig. 5 and in the Appendix. A new 1652 keV transition is found to decay into the lower 44^+ yrast state. The feeding transitions to the 46^+ terminating state are extremely weak, accounting only for approximately 20% (40% if the tentative feeding transitions are included) of the intensity decaying via the 971 keV ($46^+ \rightarrow 44^+$) transition. The 971 keV transition has an intensity of $\approx$1.5% of the 192 keV ($2^+ \rightarrow 0^+$) transition. Due to this, R measurements were not feasible for the transitions above band termination and thus assignments of multipolarities could not be made. However, R values for the transitions below band termination have been measured for the first time, which confirms the spin and parity value of the special 46^+ terminating state. In addition, a transition of energy 938 keV, which decays from the 47^- state in band 3a to the 46^+ terminating state of band 2, has been observed.

Figure 8 is a representative spectrum for band 2 from the thin-target data. This spectrum was obtained by summing up many combinations of gates requiring two transitions in the band. A list of gates was made, consisting of the 805, 845,

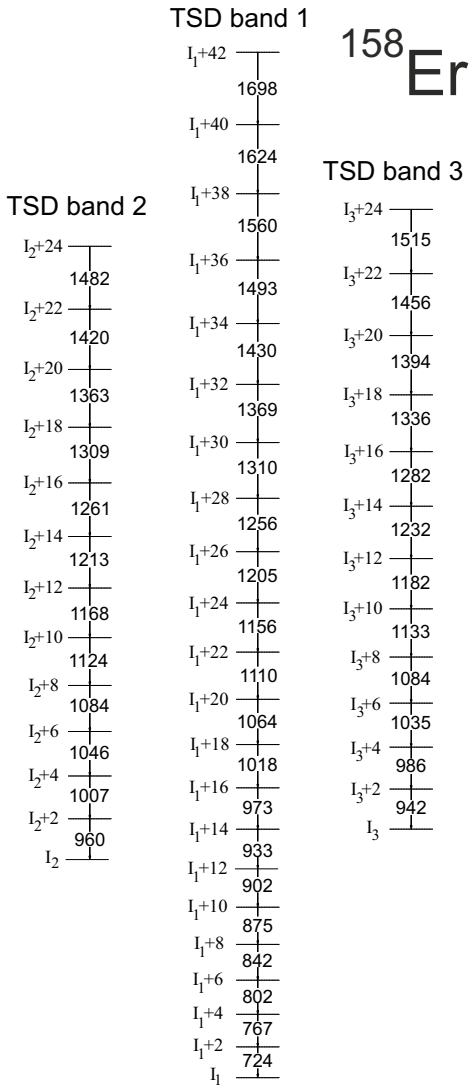

FIG. 6. The three collective TSD bands, TSD band 1, TSD band 2, and TSD band 3, which extend to ultrahigh spin, taken from Refs. [15,31,32]. Note that the spin values are rather speculative and are based on the feeding pattern of TSD band 1 to the yrast states [15]; see Sec. IV E. The suggested bandhead spins are $I_1 \approx 23$, $I_2 \approx 35$, and $I_3 \approx 36$ for TSD band 1, TSD band 2, and TSD band 3, respectively.

858, 875, 906, 959, 1017, and 1058 keV γ rays. This list of gates was double-gated with the 1030 keV ($44^+ \rightarrow 42^+$) transition. The huge drop in intensity of γ rays above the 46^+ terminating state is evident in this spectrum.

The inset of Fig. 8 has been magnified in the scale of counts with the emphasis of the γ rays in the range of 1300–2000 keV feeding into the 46^+ terminating state. This was obtained by summing up many combinations of gates on the thin-target data. Two lists of gates were created: one which included the 473, 566, 658, 740, 845, and 1058 keV γ rays and the other comprising the 971, 1030, and 1280 keV γ rays. A double-coincidence gate is set between these lists. The ten transitions feeding 46^+ are presented in Fig. 8. The transitions placed as firm (1381, 1455, 1566, 1602, 1848, and 1994 keV)

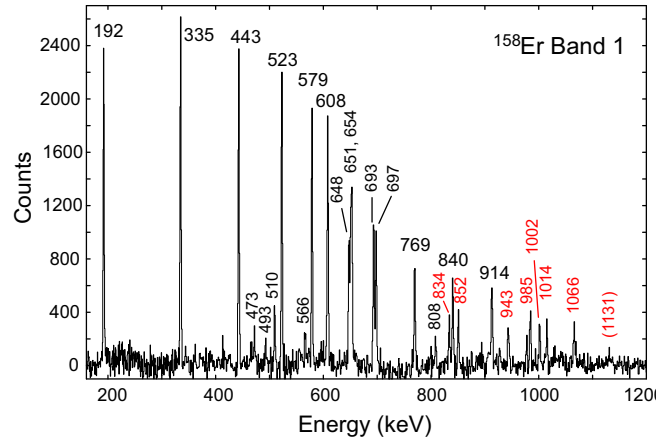

FIG. 7. Summed spectrum representative of band 1 in ^{158}Er (in coincidence with three of the transitions in this band; see text for details) from the thick-target experiment. The energies of the new transitions are highlighted in red, and previously published ones are in black. Tentative transitions are given within parentheses.

in Fig. 5 and in the Appendix are those that were also seen in the thick-target data. The tentative transitions at 1542, 1658, 1750, and 1898 keV are probably additional feeding transitions, but further data will be required to confirm this.

The unfavored part of band 2 has been extended up to the (48^+) state. However, the tentative 1274 keV γ ray

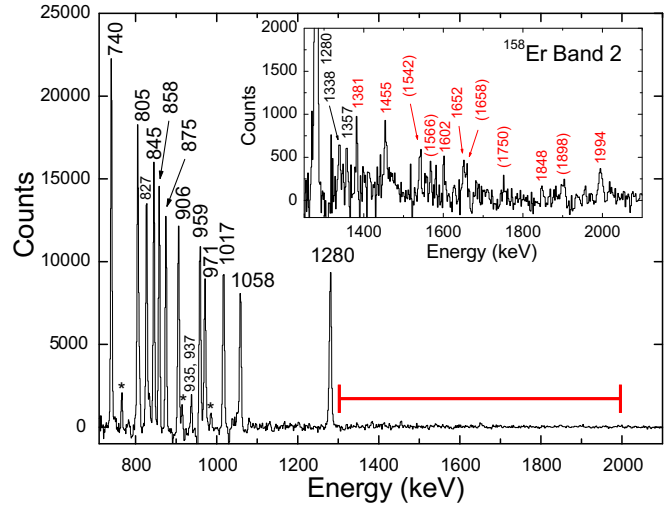

FIG. 8. High-energy part of the summed spectra representative of band 2 in ^{158}Er (in coincidence with two of the transitions in this band; see text for details) from the thin-target cube. The huge drop in intensity of γ rays above the 46^+ terminating state is evident (the 971 keV transition is the $46^+ \rightarrow 44^+$ decay). The 1300–2000 keV energy range in which the weak feeding transitions are lying is marked in a thick red line. See text for details. Inset: the high-energy region of another double-gated, summed coincidence spectrum (see text for details), shown in a magnified scale to highlight the very weak, high-energy transitions feeding into the 46^+ terminating state. Asterisks are used to denote contaminants. The labeling convention used in Fig. 7 is adopted.

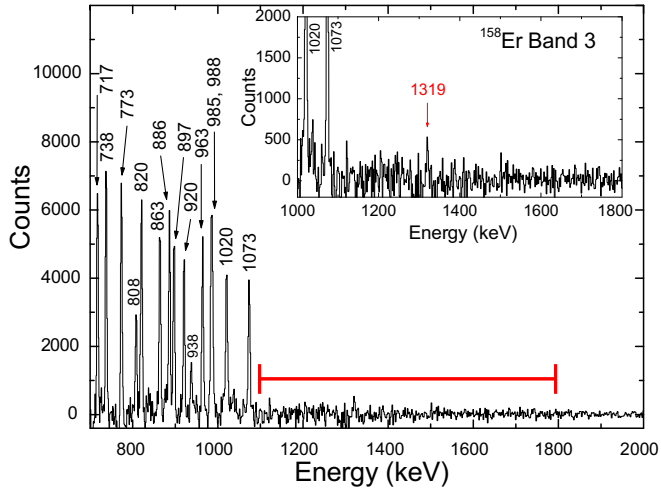

FIG. 9. High-energy part of the summed spectra representative of band 3 in ^{158}Er (in coincidence with two of the transitions in this band; see text for details) from the thin-target cube. Similar to band 2, the huge drop in intensity of γ rays above the 49^- terminating state is evident (the 808 keV transition is the $49^- \rightarrow 47^-$ decay). The 1100–1800 keV energy range in which the 1319 keV weak feeding transition is lying is marked in a thick red line. Inset: the same spectrum shown in a magnified scale for the energy range of 1000–1800 keV, in order to highlight the very weak, high-energy transition feeding into the 49^- terminating state. The labeling convention used in Fig. 7 is adopted.

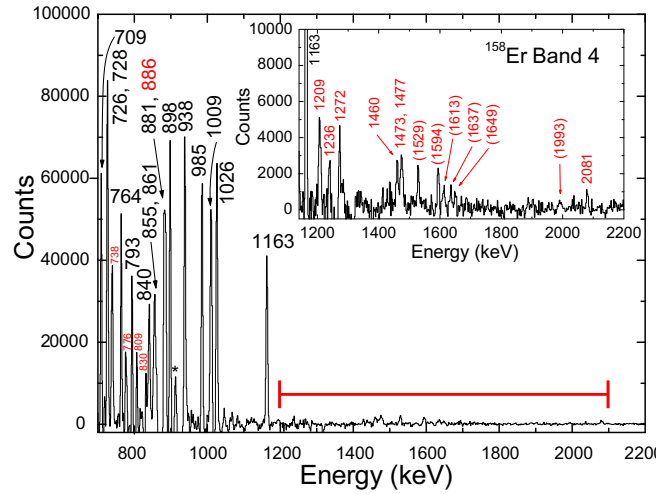

FIG. 10. High-energy part of the summed spectrum representative of band 4 in ^{158}Er (in coincidence with two of the transitions in this band; see text for details) from the thin-target cube. Similar to band 2, the huge drop in intensity of γ rays above the 48^- terminating state is evident (the 764 keV transition is the $48^- \rightarrow 46^-$ decay). The 1200–2100 keV energy range in which the weak feeding transitions are lying is marked in a thick red line. Inset: the high-energy parts of another double-gated, summed coincidence spectrum (see text for details), shown in a magnified scale to highlight the very weak, high-energy transitions feeding into the 48^- terminating state. The labeling convention used in Fig. 7 is adopted.

$(50^+ \rightarrow 48^+)$ suggested in Ref. [23] cannot be confirmed in the present work. A new transition of 983 keV from the 40^+ to the 38^+ state has been identified.

C. Band 3

Band 3 is a $(\pi = -,\ \alpha = 1)$ sequence previously observed, by Simpson *et al.* [23], up to the 49^- terminating state. In a similar manner to band 2, this band clearly demonstrates an abrupt change from a regular rotational cascade at low spin to an irregular one above the 41^- level, where the band splits into two branches. The lower energy branch from 41^- is labeled 3a in Fig. 5. One weak transition at 1319 keV was observed to feed the 49^- terminating state. It has an intensity of 20% of the 808 keV $(49^- \rightarrow 47^-)$ transition, which is ≈0.5% of the 192 keV $(2^+ \rightarrow 0^+)$ transition. This transition was also seen in the thick-target data. An R measurement could not be performed due to limited statistics and, as a result, the multipolarity of the 1319 keV γ ray could not be determined. This transition is from a state at 20 122 keV, which also populates the 48^- state of band 4a via the tentative 1993.3 keV transition. It is possible that this state could be a core-excited $I^\pi = 50^-$ state (see Sec. IVD), and is tentatively assigned as (50^-), in Fig. 5 and the Appendix. R measurements were obtained for the transitions below the 49^- band termination state. In addition, two new decays, of energies 159 and 359 keV, have been placed in the level scheme connecting the 9^- level at the bottom of band 3 to bands 1 and 6, respectively (see Fig. 3).

A representative spectrum for band 3 from the thin-target data is shown in Fig. 9. This spectrum displays a similar behavior to that of band 2, that is, there is a huge drop in intensity of γ rays above the 49^- terminating state. This spectrum was obtained by summing up many combinations of gates, each with the requirement that there were two transitions in the band. One list of gates was made including all the inband transitions from 300 to 1073 keV in band 3. This list was then double-gated with the 1330 keV $(45^- \rightarrow 43^-)$ transition. Above the 1073 keV γ ray the spectrum is relatively flat, a behavior similar to that observed in the spectrum of band 2 (Fig. 8).

D. Band 4

Band 4 is the $(\pi = -,\ \alpha = 0)$ cascade previously observed up to the 48^- terminating state [23]. This band splits into two branches at 40^-. The lower energy branch is labeled 4a in Fig. 5. Establishing the structure of this band above spin 20 was difficult, due to its complicated interaction at spins around $18\hbar$ and $30\hbar$ with band 9, discussed below. Despite this fact, four (tentatively ten) new high-energy transitions feeding into the 48^- terminating state have been found. The four firmly placed ones with energies of 1236, 1460, 1477, and 2081 keV, are included in the partial level scheme in Fig. 5 and the Appendix. The tentative γ rays of energy 1529, 1594, 1613, 1637, 1649, and 1993 keV (see Fig. 10) are probably additional feeding transitions but it will require further data to confirm this. These feeding transitions to the terminating state in band 4 are of weak intensity, similar to that observed in bands 2 and 3. The 764 keV $(48^- \rightarrow 46^-)$ transition is measured to be approximately 0.45% of the 192 keV $(2^+ \rightarrow 0^+)$

transition, and the high-energy transitions above the 48^- terminating state account only for ≈36% (tentatively 61%) of the 764 keV transition. R measurements for these very weak transitions were not possible, and thus, spin-parity assignments to their associated levels are not given. However, the R value measured for the transitions below the 48^- terminating state, confirmed the previous spin assignments suggested in Ref. [23].

Figure 10 is a representative spectrum of the high-energy region for band 4 obtained by summing many combinations of gates, each with the requirement that there were two transitions in the band. Two gate file lists were created: one comprising the 192–523 keV γ rays in the yrast band and the 840, 236–1026 keV γ rays in band 4, and the other list consisted of the 1009, 1010, and 1163 keV γ rays in band 4. A double-coincidence gate between these lists was set on the thin-target cube to produce Fig. 10. The inset of Fig. 10 is a double coincidence spectrum from the thin-target data in the region between 1200 and 2200 keV to show the feeding transitions into the 48^- terminating state. This spectrum results from a double coincidence between two lists one comprising all the in-band γ rays from 236–764 keV of band 4 and the other the 236, 385, 1009, 1010, 1026, and 1163 keV γ rays. The same procedure as in the case of band 2 has been employed to assign them in the level scheme.

The less energetically favored branch of band 4 has been extended to (44^-) in the present work. The two new γ rays of 1209 and 1272 keV can be seen in the inset of Fig. 10. The inset also shows the 1473 keV γ ray, which is placed as the $44^- \rightarrow 42^-$ transition in Fig. 5. Three new transitions with the energies of 319, 408, and 484 keV, connecting the low-spin region of band 4 with band 3, have been identified (see Fig. 3). In addition, two new transitions of 839 and 886 keV connect band 4 with band 9 at spin ≈28$\hbar$. Since R measurements were possible for band 9 (see relevant discussion below), the 839 and 886 keV γ rays have been assigned to be $\Delta I = 2$ ($E2$) transitions. Finally, a new transition of 306 keV at the bottom of band 4 has been observed. It appears to be in coincidence with the new 1057 keV γ ray, which feeds into the 6^+ level of the yrast band (see Fig. 3).

E. Bands 5, 6, and 7

Band 5 is new sequence of 11 transitions that feeds into both signatures of band 9. The spins and parity assigned to the levels of band 5 are all considered tentative due to the lack of intensity ratio R information. A representative spectrum for band 5, shown in Fig. 11, has been obtained by summing up the triple gates of c, c, and the 743 keV γ ray (the transition from the (22^-) state) set on the thick-target hypercube, excluding self-coincidences. The list c consists of the 567, 642, 692, 727, 774, and 833 keV γ rays in band 5.

Band 6, previously identified in Ref. [43] to (15^-), has been extended by four transitions to (23^-); see Fig. 12. R information could not be obtained for this band and, thus, the spins and parities of the two lowest-energy states have been taken from Ref. [43]. The higher-spin transitions are assumed to be stretched $E2$s.

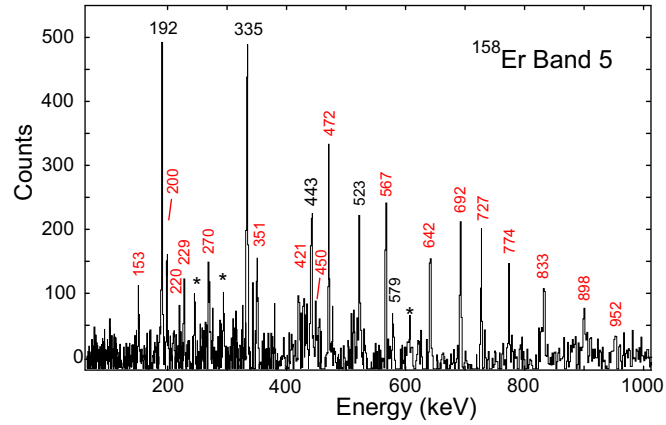

FIG. 11. Sample spectrum from the thick-target data for band 5 in ^{158}Er (in coincidence with two of the transitions in this band and the 743 keV decay γ ray; see text for details). The labeling convention used in Fig. 7 is adopted.

Band 7 is another new sequence that decays to bands 3 and 4 and at its highest spin is fed from band 9; see Fig. 4. The two linking transitions of 252 and 262 keV have been suggested to be of $\Delta I = 1$ character, based on extracted R values. This confirms the 20^- nature of the top level of band 7, since the spins and parity of band 9 were assigned with confidence. However, the spins and parities assigned to the other levels of band 7 remain tentative. The close proximity in energy of band 7 with band 9 at spin ≈20 can be see in Fig. 24 in Sec. IV. A representative spectrum for band 7 is displayed in Fig. 13. This spectrum is a double coincidence with the 786 and 499 keV γ rays from the thick-target cube.

F. Band 8

Band 8 is a new strongly coupled band that extends from (15^+) to (40^+). R measurements were possible for a few transitions confirming the nature of some of the intraband $E2$

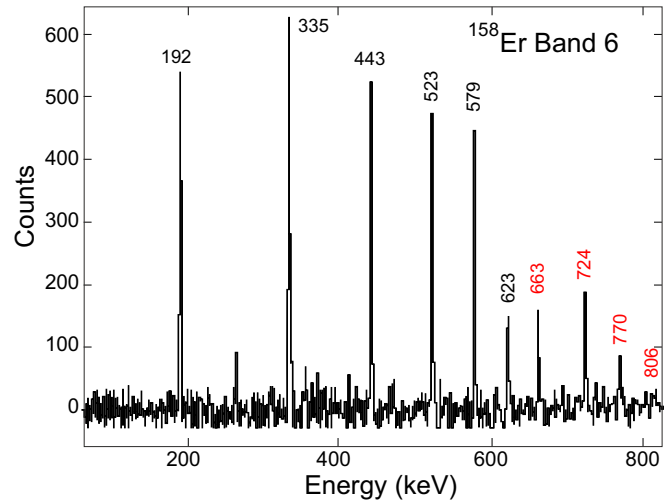

FIG. 12. Sample spectrum from the thick-target data for band 6 in ^{158}Er, selected to show the new transitions. Sum of two triple gates, one on the 608, 602, and 623, the other on the 608, 602, and 663 keV γ rays. The labeling convention used in Fig. 7 is adopted.

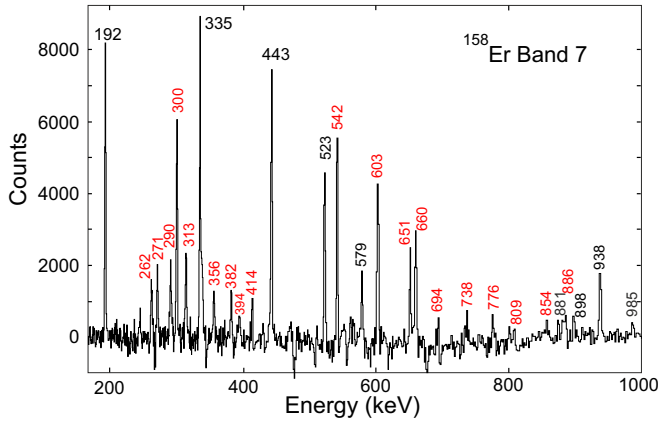

FIG. 13. Sample spectrum from the thick-target data for band 7 in ^{158}Er (in coincidence with the 786 and 499 keV transitions). The labeling convention used in Fig. 7 is adopted.

and interband dipole decays. However, since the decay-out transitions at the bottom of this band have not been established, spins and parities are tentative. Tentative transitions of 1389 and 1669 keV are observed populating the 18^+ level of band 2. There is also evidence for a tentative 999 keV γ ray feeding into the 20^+ level of band 2 (see Fig. 4). Additionally, two γ rays of 269 and 299 keV have been observed in coincidence with band 8. However, these two γ rays are not in coincidence with the 279 and 288 keV dipoles of band 8, but their sum is equal to 567 keV. Thus, they are placed in the level scheme adjacent to band 8, as shown in Fig. 4. A spectrum representative of band 8, presented in Fig. 14, has been obtained by setting a double-coincidence gate between the 311 and the 329 keV γ rays in the thick-target cube. A magnification (times 2) above 900 keV has been applied to illustrate the high-energy transitions in this band.

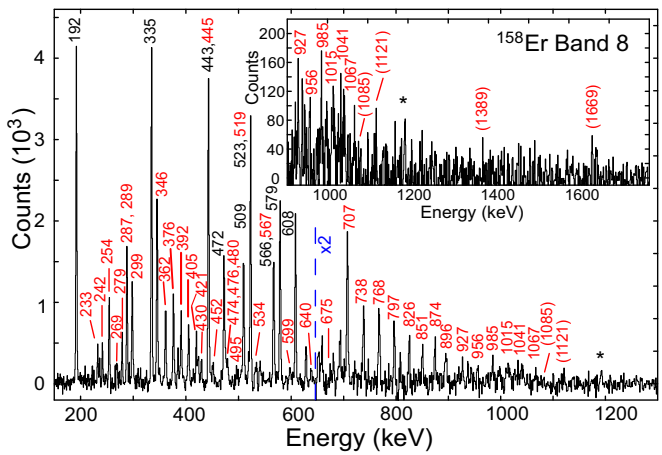

FIG. 14. Sample spectrum from the thick-target data for band 8 in ^{158}Er (in coincidence with the 311 and the 329 keV transitions in this band). In order to highlight the high-energy weak transitions in this band, the portion of the spectrum above 900 keV has been magnified (times 2) and an inset of the same spectrum for the 900–1800 keV energy range is presented. The labeling convention used in Fig. 7 is adopted.

G. Band 9

Band 9 is another new strongly coupled band observed in ^{158}Er. A total of over 55 transitions associated with band 9 have been observed. Relative to band 8, band 9 is more intense, see the Appendix. Part of band 9 was reported in Refs. [42]; however, at that time it was not possible to place this band into the level scheme of ^{158}Er. The present data established the two sequences of band 9 up to an excitation energy of (12802) keV (odd spin) and 8570 keV (even spin). R measurements have been performed for the strong intraband dipole transitions. Many cross transitions connecting band 9 to bands 1, 2, 4, 7, 10, and 11 have been observed, which enabled us to assign definite spins and parities to band 9. This was made possible by the excellent energy resolution and statistics of the thick target data. As seen in Fig. 4, the highest states in the two signatures of band 9 are 28^- and 35^-, possibly (37^-).

At the top of band 9, an 830 keV transition links this band (the even-spin sequence) to band 4 (see Fig. 4). This transition was found to have a R value of 0.97 ± 0.08, supporting its assignment of a $\Delta I = 2$ quadrupole ($E2$) transition. Since the 26^- level in band 4, where this 830 keV transition feeds into, has a known negative parity, negative parity has been assigned to band 9. The available information of other transitions linking band 9 to other bands in ^{158}Er, displayed in Figs. 3 and 4, is consistent with this assignment.

A representative spectrum for band 9 is presented in Fig. 15(a), where the complex nature of this structure may be recognized. This spectrum was obtained by setting a double-coincidence gate between the 229 and the 248 keV γ rays of band 9 in the thick-target data. Figure 15(b) is a double-coincidence gate between the 248 and the 1427 keV γ rays that shows transitions in the band above 18^-.

H. Bands 10 and 11

Band 10 and 11, see Fig. 3, are based on the previously established states that are reported in [43,46], and these gamma coincidences are confirmed. However, recent spectroscopy of these low-spin structures [47] has revised the assignment of some of the states to establish sequences based on the excited $K^\pi = 0^+$ state and the even and odd spin members of the $K^\pi = 2^+_\gamma$ gamma vibration. The 0^+, 2^+, and 4^+ states in band 10 were previously observed by Aguer *et al.* [46], and this sequence has been established up to 10^+. Band 10 is fed at low spin by decays from band 9 and at (10^+) from states in bands 2 and 3. A spectrum for band 10 that displays these connections and the 1065 keV transition from the 4^+ state to the yrast 2^+ state is presented in Fig. 16. The odd-spin sequence in band 11 was established to (9^+) in [43]. This band is fed by decays from band 9 at low spin and from band 4 at (9^+). Extensions of these bands to higher spin in Ref. [47] are not reported here.

I. Bands 12 and 13

Band 12 is a new sequence of five (seven) transitions that feeds into band 2. Due to the low intensity and the lack of R information, the spin and parity assigned to the levels of band 12 are tentative. The high-energy linking transitions that feed band 2 probably have $E1$ character; therefore, the

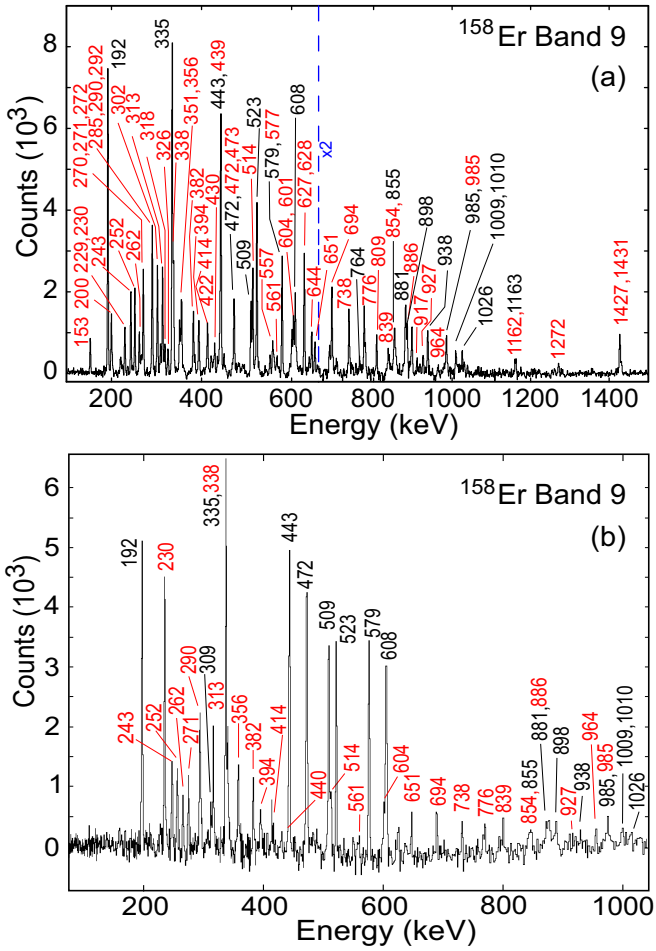

FIG. 15. Sample spectra from the thick target data for band 9 in ^{158}Er. (a) Spectrum in coincidence with the 229 and 248 keV γ rays in this band. (b) Spectrum in coincidence with the 248 keV transition in this band and the 1427 keV that connects this band to band 2. The labeling convention used in Fig. 7 is adopted.

highest observed spin for band 12 is (33^-), possibly (37^-). A spectrum for band 12 is shown in Fig. 17, and has been obtained by setting a triple gate on two lists and the 1090 keV (the transition from the (23^-) state). One list is the yrast band up to the 22^+ state and the other is made up of transitions in band 12 to the (35^-) state.

Band 13 is another new band with four (tentatively five) transitions from (20^-) to (30^-) that decays via a 755 keV transition to band 4 at 18^-. R measurements could not be performed for this band, therefore the spin and parity assignments are tentative. A spectrum representative of band 13 is shown in Fig. 18, which has been obtained by setting a triple gate on the 755 keV, a list comprising the 730, 800, 857, and 914 keV γ rays in band 13, and a list comprising the 236, 385, 519, 629 and 709 γ rays in band 4.

J. Collective bands at spins beyond band termination

Three rotational band structures displaying high dynamic moments of inertia were observed in ^{158}Er [15,30–32], and are labeled TSD band 1, TSD band 2, and TSD band 3 in Fig. 6.

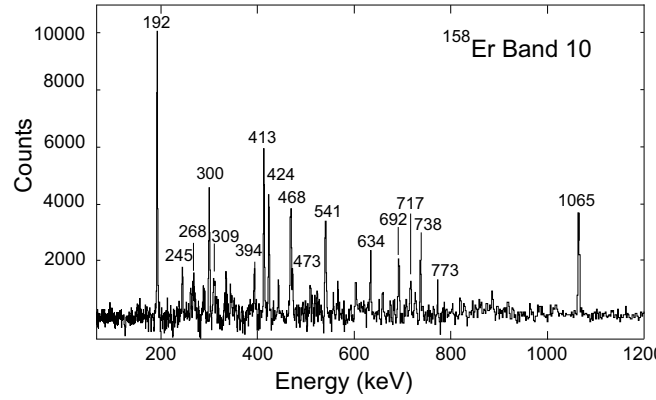

FIG. 16. Spectrum in coincidence with the 331 and 429 keV transitions in band 10 from the thick-target data.

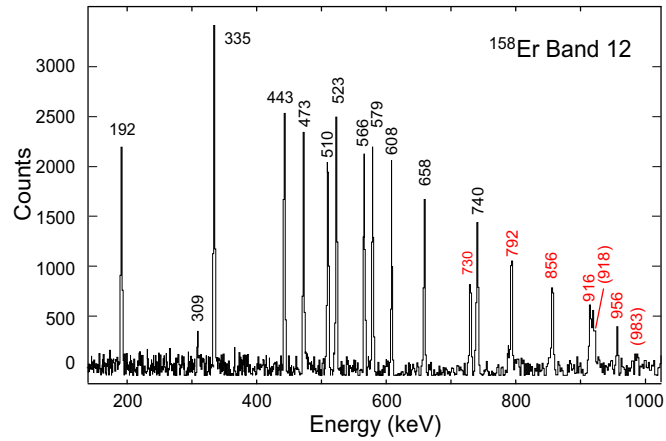

FIG. 17. Sample spectrum from the thick-target data for band 12 in ^{158}Er (in coincidence with the 1090 keV decay, yrast band transitions and transitions in band 12; see text for details). The labeling convention used in Fig. 7 is adopted.

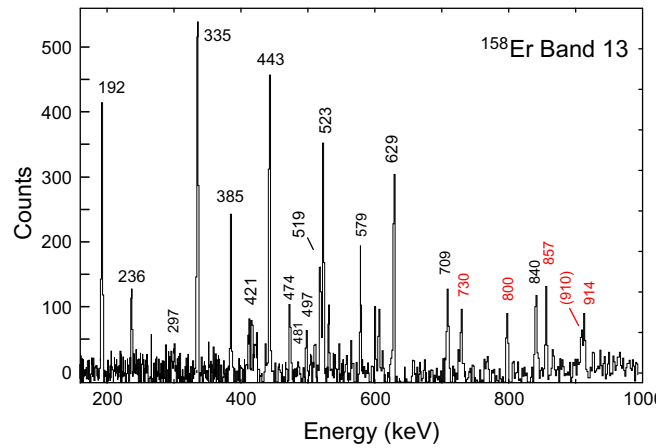

FIG. 18. Sample spectrum from the thick-target data for band 13 in ^{158}Er (a triple gate between the 755 keV decay, transitions in band 13 and transitions in band 4; see text for details). The labeling convention used in Fig. 7 is adopted.

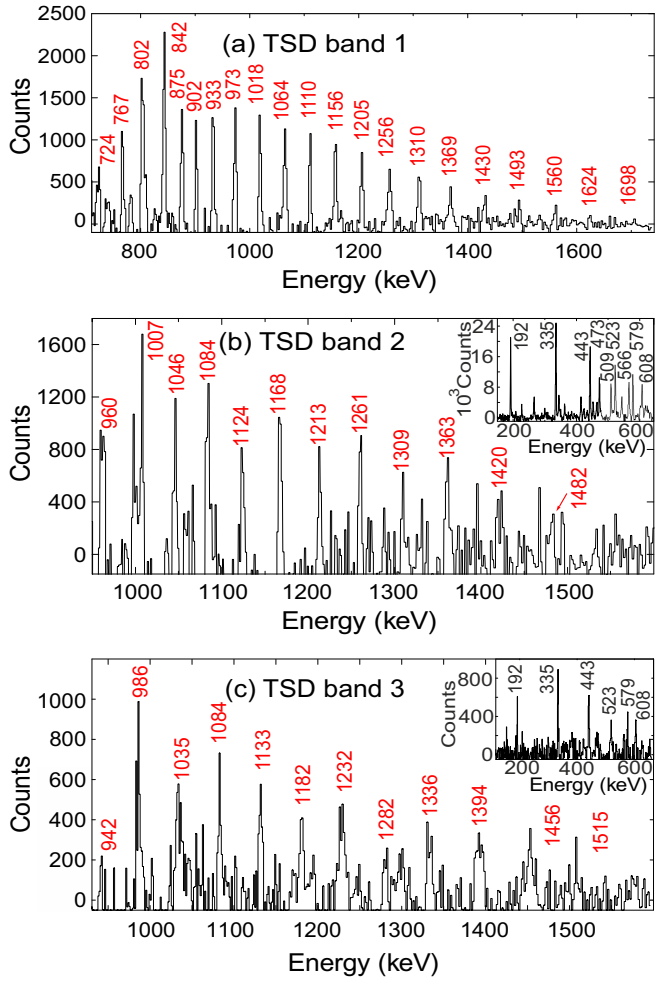

FIG. 19. Multicoincidence γ-ray spectra for the three TSD structures. These spectra were adapted from [15,31,32]. TSD band 1 (a) and TSD band 2 (b) are from the thin-target data and TSD band 3 (c) is from the thick-target data. The insets for (b) and (c), both from the thin-target data, display the low energy region of the spectra confirming that TSD band 2 and TSD band 3 are in ^{158}Er. The decay profile of TSD band 1 into the ^{158}Er yrast states can be found in Ref. [15].

Representative spectra for these bands are shown in Fig. 19. TSD band 1 (a) and TSD band 2 (b) are from the thin-target data and TSD band 3 (c) is from the thick-target data. The γ-ray energies are listed in the Appendix, Table V. An analysis of the intensity profile of TSD band 1, in comparison to the observed feeding intensities into the known normal deformed yrast states, allowed an estimation of possible spin values in TSD band 1 (and thus subsequently TSD band 2 and TSD band 3), with the suggestion that it tentatively extends up to spin $\approx 65\hbar$ [15]. All three bands have very low intensities, with TSD band 1 being $\approx 10^{-4}$ of the intensity of the yrast $2^+ \rightarrow 0^+$ transition. TSD band 2 is 2–3 times lower in intensity than TSD band 1 and TSD band 3 a factor of ≈ 10 lower. The insets for Figs. 19(b) and 19(c), both from the thin-target data, display the low energy region of the spectra confirming that TSD band 2 and TSD band 3 are in ^{158}Er. In spite of their extremely low intensities, an analysis of fractional Doppler shifts, $F(\tau)$, was conducted for the three collective bands at ultrahigh spin in ^{158}Er. Their transition quadrupole moments were experimentally determined to be TSD band 1: $11.7^{+0.7}_{-0.8}$ eb; TSD band 2: $11.1^{+1.3}_{-1.0}$ eb; and TSD band 3: $9.6^{+1.5}_{-1.1}$ eb (see Refs. [12,31,32] for further details).

TABLE I. Quasiparticle-labeling scheme for ^{158}Er based on the predominant Nilsson components at $\hbar\omega = 0$ MeV and their parity and signature (π, α). Adapted from [52].

	Label	$(\pi, \alpha)_n$	Nilsson orbital
Quasineutrons	A	$(+, +1/2)_1$	[651]3/2
	B	$(+, -1/2)_1$	[651]3/2
	C	$(+, +1/2)_2$	[660]1/2
	D	$(+, -1/2)_2$	[660]1/2
	E	$(-, +1/2)_1$	[523]5/2
	F	$(-, -1/2)_1$	[523]5/2
	G	$(-, -1/2)_2$	[521]3/2
	H	$(-, +1/2)_2$	[521]3/2
	X	$(-, -1/2)_3$	[505]11/2
	Y	$(-, +1/2)_3$	[505]11/2
Quasiprotons	A_p	$(-, -1/2)_1$	[523]7/2
	B_p	$(-, +1/2)_1$	[523]7/2
	C_p	$(-, -1/2)_2$	[532]5/2
	D_p	$(-, +1/2)_2$	[532]5/2
	E_p	$(+, -1/2)_1$	[404]7/2
	F_p	$(+, +1/2)_1$	[404]7/2
	G_p	$(+, +1/2)_2$	[402]5/2
	H_p	$(+, -1/2)_2$	[402]5/2
	I_p	$(+, -1/2)_3$	[411]1/2
	J_p	$(+, +1/2)_3$	[411]1/2
	X_p	$(-, +1/2)_4$	[541]1/2

IV. DISCUSSION

The behavior with increasing angular momentum (up to $\approx 40\hbar$) can be understood in terms of rotational alignments of quasiparticle pairs in a prolate-deformed collectively rotating nucleus. Observation of neutron and proton alignments in ^{158}Er was in fact helpful for placing the cranked shell model [48–50] on a firm footing, see for example Refs. [12,42,43,51]. A brief summary of observed alignments of bands 1, 2, 3, and 4 is given since this is helpful to understand the alignment behavior, and thus quasiparticle configuration, of the two new strongly coupled structures, bands 8 and 9, as well as the other new rotational sequences. The discussion will then focus on the behavior at higher spins of bands 2, 3, and 4, as they approach band termination.

A. Collective rotational structures at spins below band termination

The quasiparticle labeling scheme adopted in the present work is given in Table I. Figure 20(a) shows a plot of the experimental alignment i_x [49], as a function of rotational frequency $\hbar\omega$ for bands 1, 2, 3, and 4. In order to perform comparisons between the alignment behavior seen in different

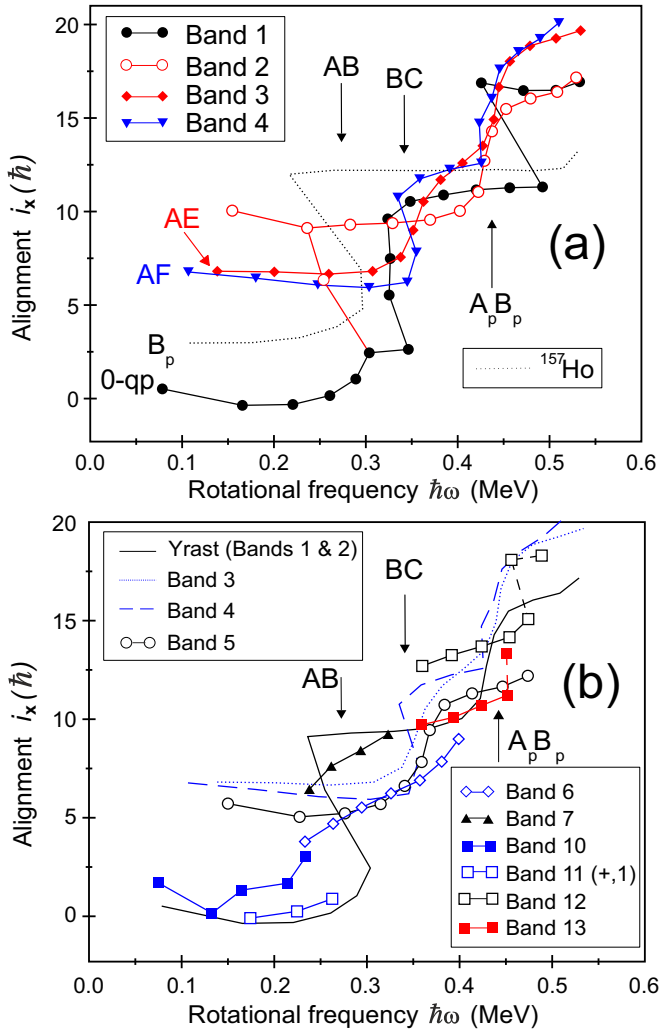

FIG. 20. (a) Experimental alignment (i_x) as a function of the rotational frequency ($\hbar\omega$) for bands 1–4 in ^{158}Er. The band with the B_p configuration in ^{157}Ho, used as the reference, is plotted as a thin black dotted line. The structures are labeled according to their quasiparticle configurations at low spin. The band crossings are labeled at the approximately corresponding rotational frequencies. (b) Experimental alignment (i_x) as a function of the rotational frequency ($\hbar\omega$) for bands 1–7, 10, 11 (odd spin), 12–13 in ^{158}Er. Bands 3, 4 and the yrast band are shown as thin lines. The approximate rotational frequency of the various band crossings is indicated.

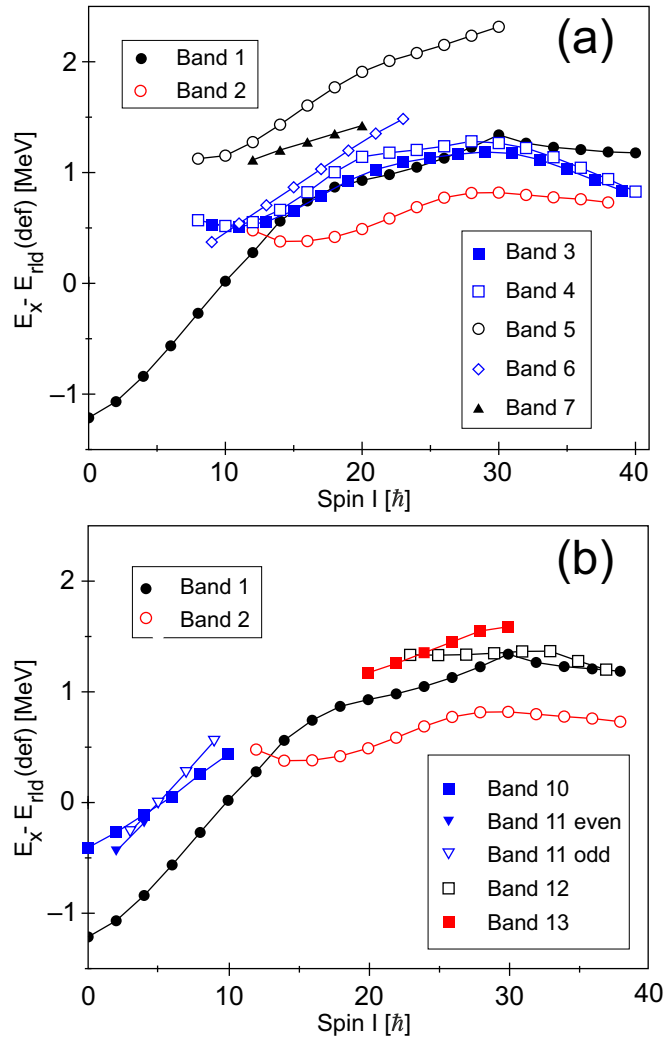

FIG. 21. Experimental excitation energy, minus a deformed rotating liquid drop reference [13,14], plotted as a function of spin for (a) bands 1–7 and (b) bands 1, 2, 10–13 in ^{158}Er, including the even and odd spin sequences of band 11.

isotopes, it is important to adopt an appropriate rotational reference to be subtracted. A rotational reference with Harris parameters [53] $\mathcal{J}_0 = 32$ MeV$^{-1}\hbar^2$ and $\mathcal{J}_1 = 34$ MeV$^{-3}\hbar^4$ was used. This choice of the Harris parameters gives a constant alignment for the $(-, +1/2)$ three-quasiparticle configuration (B_pAB) in the odd-proton neighboring nucleus ^{157}Ho [illustrated by a dotted line in Fig. 20(a)]. The reference is convenient when comparing the high-spin alignment properties in the same and neighboring nuclei, since the second and third neutron $i_{13/2}$ crossings BC and AD, as well as the first and second $h_{11/2}$ proton alignments A_pB_p and B_pC_p, are blocked for this configuration. An additional $i_o = 1.6\hbar$ offset was added to the alignment to ensure that band 1 (ground-state band) has on average approximately zero alignment at low rotational frequencies (the first four transitions).

Band 1 is the zero-quasiparticle (0-qp) sequence, which is yrast until the alignment of the first pair of $i_{13/2}$ quasineutrons (AB). At higher spins, $I > 12$, band 2 becomes the yrast sequence (see Fig. 21). As displayed in Fig. 20, the AB crossing occurs at $\hbar\omega \approx 0.28$ MeV and has a gain of alignment $\Delta i_x \approx 10\hbar$. This increase is the same as seen in the B_p structure in the neighboring odd-proton isotone ^{157}Ho [54,55]. The portion of band 1 above the 12^+ level is the continuation of the 0-qp sequence. The band gains significant alignment, which is greater than the two quasineutron configuration AB (band 2) above $\hbar\omega \approx 0.35$ MeV. This has been interpreted as consecutive second and third band crossings of $i_{13/2}$ quasineutrons (BC and AD) [43,56–59].

The next lowest two-quasineutron configurations in ^{158}Er are formed by one quasineutron occupying the A orbital (lowest energy, positive parity), and the other quasineutron occupying the next lowest in energy, negative-parity orbitals,

E or F. In this way, the AE and AF configurations, which have negative parity and signatures of 1 and 0, were assigned to bands 3 and 4, respectively (see Fig. 21). The first observed alignment in bands 3 and 4, at $\hbar\omega \approx 0.36$ and $\approx$0.35 MeV, respectively, has been interpreted as a BC crossing [51], as displayed in Fig. 20.

At higher rotational frequencies, $\hbar\omega \approx 0.43$ MeV, the alignment of the first pair of $h_{11/2}$ quasiprotons (A_pB_p) occurs (see Fig. 20) with an expected gain in alignment of about $6\hbar$ in bands 1, 2, 3, and 4. At this point, the configuration of band 2 changes from AB to ABA_pB_p, while for bands 1, 3, and 4 the 4-qp configurations evolve to 6-qp configurations ($BCAD \rightarrow BCADA_pB_p$ for band 1, $AEBC \rightarrow AEBCA_pB_p$ for band 3, and $AFBC \rightarrow AFBCA_pB_p$ for band 4). The experimental evidence for the interpretation of the A_pB_p rotational alignment is that similar anomalies occur in all the yrast and non-yrast rotational bands of neighboring even-proton nuclei, but not in the yrast bands of the neighboring odd-proton nuclei (such as ^{157}Ho [54,55]), where this alignment is Pauli blocked. Additional confirmation comes from the fact that the A_pB_p alignment is observed in non-yrast rotational bands in odd-proton nuclei, for example ^{157}Ho [54,55].

At low rotational frequency bands 5, 6, and 7 have an alignment consistent with a two-quasiparticle structure, see Fig. 20(b). These bands gain an alignment at a frequency close to the BC crossing as observed in bands 3 and 4. The next three most favored two-quasineutron configurations after AE (band 3) and AF (band 4) are AG, AH, and BE. Band 5 is interpreted as the AG $(-, 0)$ configuration and is observed through the BC crossing established at $\hbar\omega \approx 0.36$ MeV, closely following the behavior of band 3 and 4. Band 6 is tentatively assigned as the AH $(-, 1)$ configuration. Band 6 lies at a relatively low energy compared with its signature partner band 5; see Fig. 21. This is opposite to the expectation from the cranked shell model, however, as noted in [43], this band may interact with a $K = 0$ octupole-vibrational band at low spins, which would lower its energy. Similar bands are observed in neighboring nuclei (e.g., [52,59]). Band 6 smoothly gains alignment [see Fig. 20(b)], which could be evidence for the BC crossing. Band 7 $(-, 0)$ is tentatively interpreted as the next two-quasineutron configuration BE. Its interaction with band 9 near $I = 20$ means that it is not seen to high enough spin to observe the BC crossing.

B. Strongly coupled structures

Bands 8 and 9 are strongly coupled structures consisting of interleaved, energetically degenerate, rotational sequences connected by interlinking $M1/E2$ $\Delta I = 1$ dipole transitions. Such structures arise when there is a significant contribution of single-particle angular momentum aligned along the intrinsic nuclear deformation axis (z axis), which is perpendicular to the rotational x axis. This occurs for nucleons at the Fermi surface that reside in Nilsson states with large Ω values, i.e., states near the top of a major oscillator shell. The overall nuclear spin vector $\vec{I}$, and hence its associated magnetic dipole moment vector, are tilted away from the rotational x axis leading to enhanced $M1$ emission.

For erbium ($Z = 68$) isotopes, available high-Ω proton states correspond to [404]7/2 and [402]5/2 Nilsson orbitals (the E_p/F_p and G_p/H_p states of Table I). Also for $N = 90$ the high-Ω neutron orbital [505]11/2 (the X/Y states of Table I) is near the Fermi surface (e.g., [60]). Hence, there is the possibility of observing both proton and neutron strongly coupled bands in ^{158}Er.

Strongly coupled bands have been systematically observed in neighboring even-A and odd-A erbium isotopes, and in several cases multiple bands are seen. These bands have been associated with both proton and neutron high-K configurations (e.g., [61]). In particular, strongly coupled bands built on an $I^\pi = 7^-$ two-quasiproton state, namely [523]7/2 $\otimes$ [404]7/2 or $A_p(E_p/F_p)$, are well established in several nuclei in the $_{68}$Er, $_{70}$Yb, and $_{72}$Hf region with neutron numbers between 90 and 96, e.g,. [62]. Band 9 in ^{158}Er is therefore an obvious candidate for this proton configuration as it has all the characteristics expected (i.e., alignment properties, $B(M1)/B(E2)$ values), see below. In addition, neighboring odd-N ^{157}Er [63] and ^{159}Er [64,65] exhibit related bands based on this A_pE_p/F_p high-K structure coupled to the odd neutron in the A orbital ($i_{13/2}$).

One way to easily distinguish between high-K proton and neutron strongly coupled configurations is to extract $B(M1; I \rightarrow I-1)/B(E2; I \rightarrow I-2)$ ratios of reduced transition probabilities and to compare them with theoretical expectations. The experimental ratios are simply related to the intensity branching ratios of interband dipole ($\Delta I = 1$) and intraband quadrupole ($\Delta I = 2$) γ rays depopulating a particular state. The best way to obtain reliable intensity branching ratios is to set coincident gates above the level of interest and then measure the relative intensities of the competing dipole and quadrupole transitions depopulating that level. The theoretical estimates used are based on the semiclassical geometrical model of Dönau and Frauendorf [66,67] along with Nilsson single-particle g factors [68].

The high-Ω states are relatively pure and these g-factors approach the spherical shell-model values. It is found that high-K proton configurations are predicted to yield much larger (5–10 times) $B(M1)/B(E2)$ values than neutron configurations and, when compared with the experimental values, imply that the two strongly coupled bands in ^{158}Er are indeed both built on high-K proton excitations. The experimental $B(M1)/B(E2)$ values for bands 8 and 9 are shown in Fig. 22 where they are compared with various theoretical high-K proton configurations. Some experimental $B(M1)/B(E2)$ values are missing in this figure because of the difficulty of extracting meaningful γ-ray intensities due to contamination.

The systematics in the region and alignment properties, see below, suggest that band 9 is the negative-parity $A_p(E_p/F_p)$ two-quasiproton configuration, involving the [404]7/2 Nilsson state, at low spin, which then evolves into the four-quasiparticle $A_p(E_p/F_p)AB$ configuration following the rotational alignment of $i_{13/2}$ neutrons. These are the calculated configurations labeled 5 and 6 in Fig. 22(b). The $I^\pi = K^\pi = 7^-$ state at 2402 keV is taken to be the bandhead of band 9. Although there is a lower state with $I^\pi = 6^-$ at 2132 keV, its low excitation energy and the unusually large $B(M1)/B(E2)$ value

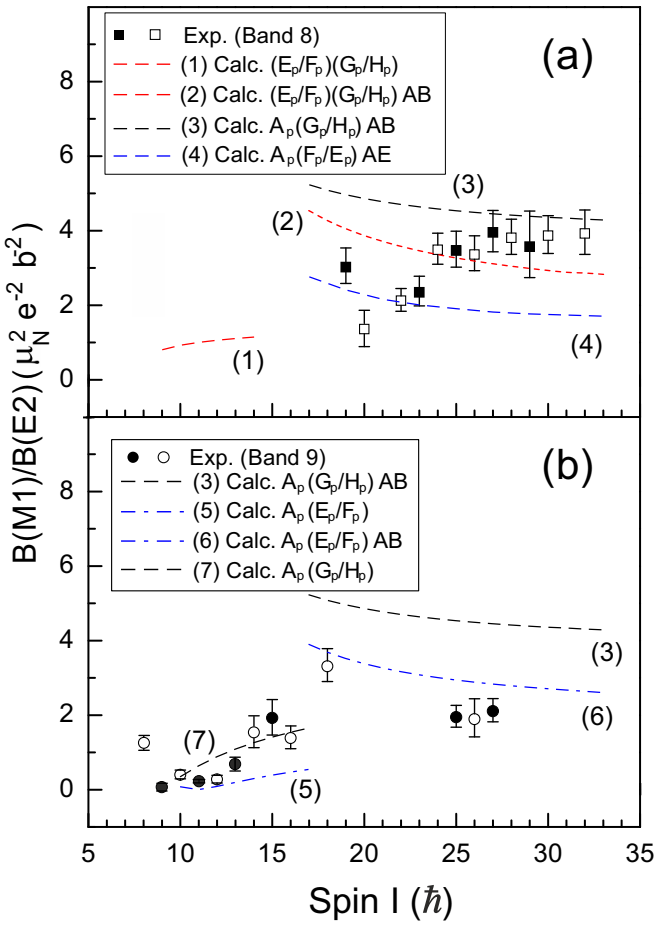

FIG. 22. Measured $B(M1)/B(E2)$ ratios of reduced transition probabilities as a function of spin for bands 8 (top panel) and 9 (bottom panel) in ^{158}Er. Open (filled) symbols denote the signatures $\alpha = 0$ (1). The configurations for the theoretical calculations are given in the boxes.

for $I = 8$ suggest this 6^- state is not part of the same configuration. Band 9 could also be the $A_p(G_p/H_p)$ configuration at low spin based on the $B(M1)/B(E2)$ values and alignment properties. However, at higher spin the $A_p(E_p/F_p)AB$ configuration is the best overall fit to the data and therefore band 9 is assigned to be the $A_p(E_p/F_p) \rightarrow A_p(E_p/F_p)AB$ configuration.

Band 8 exhibits relatively large $B(M1)/B(E2)$ values of $\approx 4(\mu_N/eb)^2$ above spin $25\hbar$. These values are larger than those systematically observed in this region. Four-quasiparticle strongly coupled bands, based on the positive-parity $A_p(E_p/F_p)AE$ mixed proton-neutron configuration have been established in ^{160}Er [61] and ^{164}Er [69]. In the latter case the bandhead is isomeric with a lifetime of $\approx$100 ns. Calculations for the corresponding configuration in ^{158}Er are included in Fig. 22(a) labeled 4. Although these calculations match the values extracted for spins below $I = 24$, the experimental numbers are significantly larger at higher spin values. Indeed, at high spin the behavior of band 8 is best described by the positive-parity four-quasiparticle $(E_p/F_p)(G_p/H_p)AB$ configuration, labeled 2 in Fig. 22(b), which involves both [404]7/2 and [402]5/2 high-K proton orbitals coupled to rotational aligned $i_{13/2}$ neutrons. In this particular configuration, the proton spin is essentially all aligned along the intrinsic nuclear deformation axis, while the neutron spin is aligned with the perpendicular rotation axis. This arrangement naturally leads to enhanced $M1$ γ-ray emission.

The proton assignment to the two ^{158}Er strongly coupled bands is consistent with detailed theoretical discussion of quasiproton configurations (excitation energies, deformations, alignments, and band crossing properties) calculated by Bengtsson in Ref. [70], where the existence of such bands had been theoretically predicted. Moreover, the proton structure of the bands can also be confirmed by comparing their rotational properties to neighboring odd-Z ^{157}Ho [55]. Figure 23(a) shows the alignment as a function of rotational frequency for the bands compared with the yrast states in bands 1 and 2, while Figs. 23(b) and 23(c) show the bands compared with one-quasiproton bands in ^{157}Ho. Figure 24(a) shows the excitation energy with respect to a deformed rotating liquid drop reference for the strongly coupled bands compared with the yrast states in bands 1 and 2. Figure 24(b) shows the excitation energy with respect to a deformed rotating liquid drop reference for the yrast states of bands 1 and 2 with the $(-, 0)$ even spin states in the negative-parity bands 4, 7, 9, and 13. The close interaction with band 9 and 7 at spins 12 and 20 and between band 4 and 13 at spin 20 is clearly evident explaining the decays between these bands, see Figs. 3, 4, and 24(b).

In Fig. 23(c), band 9 follows a very similar trajectory with the B_p sequence in ^{157}Ho. This is consistent with a proton configuration at low rotational frequency. Considering the small signature splitting ($\leqslant$ 20 keV) between the two partner sequences of band 9 (see Fig. 24), this band is based on the configurations A_pE_p and A_pF_p. This configuration assignment is consistent with the fact that the initial aligned spin of band 9 is almost identical to the sum of those of the A_p sequence and the E_p or F_p sequence in ^{157}Ho [see Fig. 23(c)]. Furthermore, band 9 in ^{158}Er displays an alignment pattern similar to the A_p sequence in ^{157}Ho. As seen in Figs. 20 and 23(c), both the A_p and B_p sequences in ^{157}Ho encounter the AB quasineutron crossing at $\hbar\omega \approx 0.27$ MeV. At higher rotational frequencies, an alignment of the first pair of quasiprotons (A_pB_p) is expected, as observed in the yrast band (band 2) in ^{158}Er at $\hbar\omega \approx 0.43$ MeV. However, this alignment is blocked in band 9 which already contains the A_p quasiproton, but the next alignment of the second and third quasiprotons B_p and C_p is observed at $\hbar\omega \approx 0.47$ MeV. It should be noted that at these high rotational frequencies the orbital X_p, originating from the $h_{9/2}[541]1/2$, is low in energy and may be involved in this alignment.

Band 8 in ^{158}Er exhibits a gradual gain in alignment over a large frequency range $0.20 < \hbar\omega < 0.55$ MeV; see Fig. 23(a). Similar behavior is seen in the corresponding bands of ^{157}Ho, shown in Fig. 23(b), and has also been observed in the neighboring even-even nuclei ^{156}Dy and ^{158}Dy, where it has been interpreted as the rotational alignment of the A_pB_p quasiprotons with a large interaction strength; see Refs. [59,71]. If this

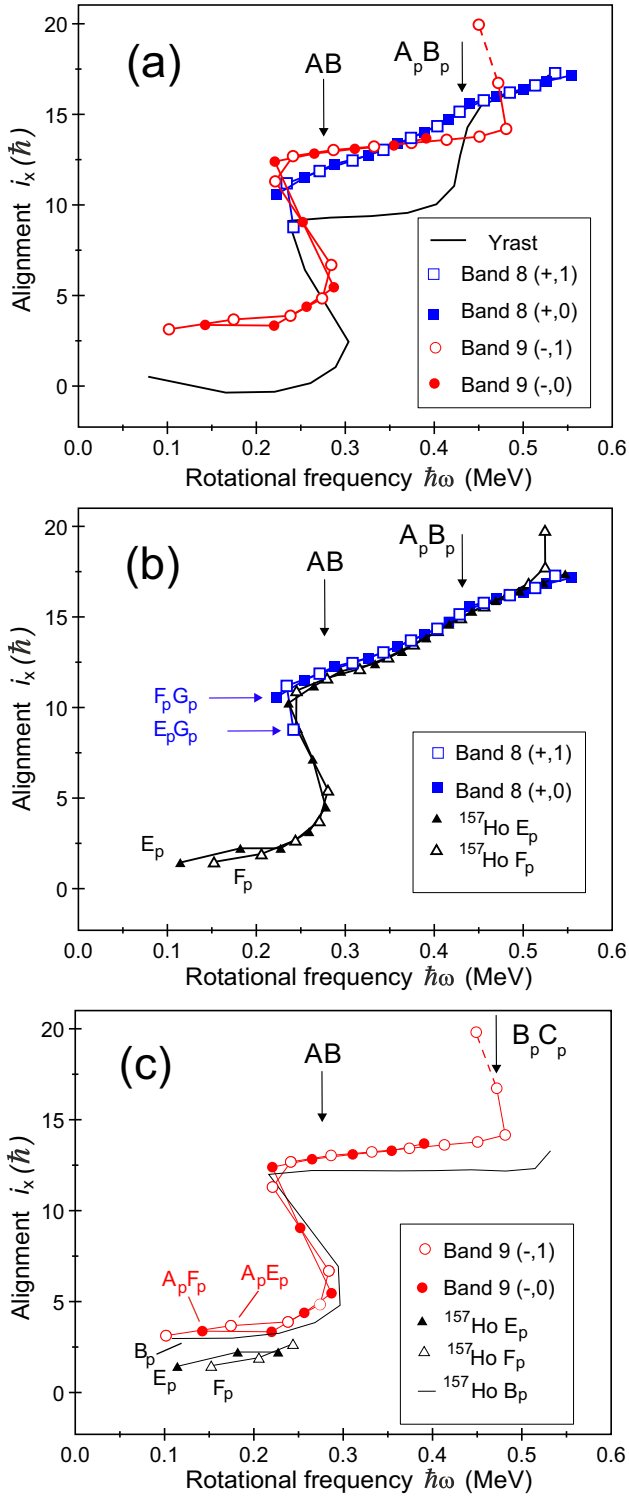

FIG. 23. Experimental alignments (i_x) as a function of the rotational frequency ($\hbar\omega$) for the two strongly coupled bands observed in ^{158}Er; band 8 and band 9. (a) Comparison of bands 8 and 9 with the yrast states in bands 1 and 2. In (b) and (c) the related configurations in ^{157}Ho are plotted. The structures are labeled according to their quasiparticle configurations at low spins. The approximate rotational frequency of the various band crossings is indicated. Open (filled) symbols denote the signatures $\alpha = +1/2$ $(-1/2)$ or 0 (1). See text for details.

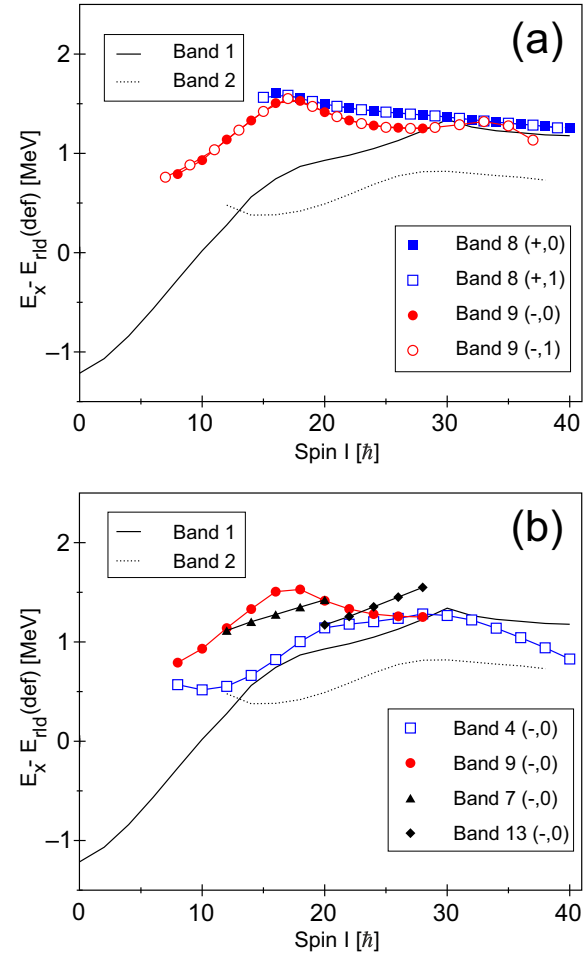

FIG. 24. Experimental excitation energy, minus a deformed rotating liquid drop reference, plotted as a function of spin for (a) bands 8 and 9 in ^{158}Er and (b) the even spin states in band 9 and bands 4, 7, and 13 in ^{158}Er. Bands are labeled by the parity and signature (π, α). Bands 1 and 2 are displayed as a reference.

interpretation is adopted for band 8 of ^{158}Er, it represents a very smooth and gradual upbend centered at $\hbar\omega \approx 0.42$ MeV with a total gain in alignment of $\approx 6\hbar$.

The dynamic moment of inertia of band 8, $\mathcal{J}^{(2)} \approx$ 60–70 MeV/$\hbar^2$, is larger than that of band 9, which has a value of $\approx$45–50 MeV/$\hbar^2$. This is shown in Fig. 25 which compares the moments of inertia in several bands in ^{158}Er together with selected structures in other nuclei. The higher value of the $\mathcal{J}^{(2)}$ in band 8, which is close to the triaxial superdeformed band in ^{163}Lu [74,75], is caused by the gradual A_pB_p alignment. Band 9, where the A_pB_p alignment is blocked, has a $\mathcal{J}^{(2)}$ value more typical of lower-deformed structures.

Finally, dipole transitions are observed from band 4 (AF) to band 3 (AE), allowing experimental $B(M1)/B(E2)$ ratios to be measured for these bands and compared with theory. Experimental values of ≈ 0.02 $(\mu_N/eb)^2$ are found, which are an order of magnitude smaller than those of bands 8 and 9; see Fig. 22. However, these lower values are consistent with our predictions, using the semiclassical geometric model [66,67],

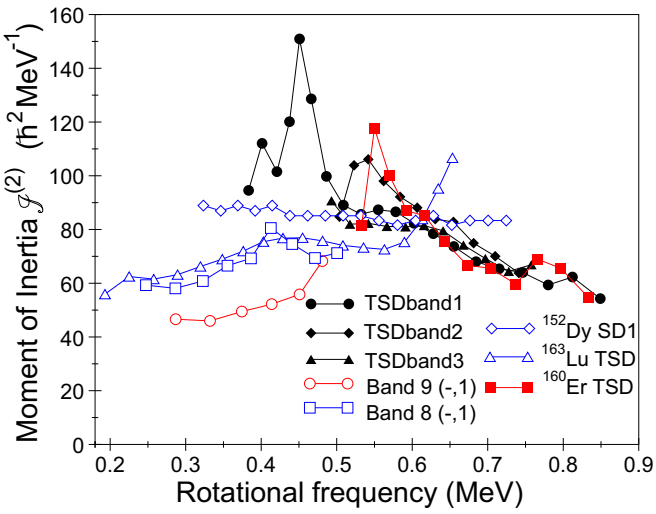

FIG. 25. The dynamic moment of inertia $\mathcal{J}^{(2)}$ as a function of rotational frequency for the three TSD bands in ^{158}Er. The lowest energy superdeformed band in ^{152}Dy [72,73], the lowest energy triaxial strongly deformed band in ^{163}Lu [74,75] and ^{160}Er [76], and the strongly coupled bands 8 (−, 1) and 9 (−, 1) in ^{158}Er are plotted.

for the expected $[651]3/2 \otimes [523]5/2$ two-quasineutron configuration for these negative-parity bands.

C. Other bands

Band 10 is based on excited 0^+, 2^+, and 4^+ states identified by Aguer *et al.*, [46], where they were interpreted as the $K^\pi = 0^+$ β-vibrational band. Similar bands are observed in many nuclei in this region (e.g., ^{154}Gd [77] and ^{156}Er [78]). However, the interpretation of these bands has been questioned [77,79]. Indeed, the recent work of Dinoko et al., [47] interprets band 10 as a "pairing isomer" or states forming a second vacuum [77,80] and thus based on an excited $K^\pi = 0^+$ state. This band would be expected to undergo the AB quasineutron alignment as observed in the yrast states [see Fig. 20(b)] and in neighboring nuclei (e.g., ^{156}Er [78]). However, it is not observed to high enough spin to confirm this expectation.

Band 11 is interpreted as comprising the even and odd spin members of the $K^\pi = 2^+_\gamma$ γ-vibrational band [46]. This assignment is consistent with the fact that these two sequences are close in excitation energy, as shown in Fig. 21(b). Band 10 and 11 have been extended to higher spin by Dinoko *et al.* [47], who present a detailed discussion of their structure.

The alignment plot for the new bands 12 and 13 are plotted in Fig. 20(b) and their excitation energy with respect to a deformed rotating liquid drop reference is plotted in Fig. 21(b). Band 12 is only observed at frequencies >0.36 MeV and has large values of aligned spin 12–14 $\hbar$. Since the A_pB_p alignment appears to be missing in band 12, it is tentatively suggested to be the four-quasiparticle structure (two quasineutrons and two quasiprotons), I_pA_pAB, in the range of observed frequencies.

Band 13 has an alignment close to that of band 1 after its continuation beyond the AB crossing, where it is interpreted as the four-quasineutron configuration $BCAD$; see Table II. Band 13 could also be a four-quasineutron configuration and is tentatively assigned to be $BEAD$. Its excitation energy lies slightly higher than band 1 (see Fig. 24), which is consistent with cranking calculations; see for example in [43], where the C orbital lies at higher energy than the E orbital.

D. Band termination

At high spin in bands 2, 3, and 4, parallel structures are observed, labeled in Fig. 5 as bands 2a, 3a, and 4a, respectively. These latter structures become yrast at the highest spins. This feature has been interpreted as a crossing of near-prolate collective rotational structures by energetically favored, weakly collective sequences, which terminate into a noncollective oblate shape; see Refs. [7,8,12,20,21,23–27]. These references have gone into extensive detail with regard to the highly favored band-terminating states, at $I^\pi = 46^+$, 48^-, and 49^-, together with their interpretation in terms of fully aligned configurations involving the four valence protons and eight neutrons outside the ^{146}Gd core. These terminating states correspond to *valence-space* configurations. States at

TABLE II. A summary of the assignments to the bands in ^{158}Er including proposed quasiparticle configurations. See Table I for quasiparticle labeling scheme and associated predominant Nilsson components.

Band no.	(Parity, Signature)	Configuration
Band 1	(+, 0)	$0 \rightarrow BCAD \rightarrow BCAD \otimes A_pB_p$
Band 2	(+, 0)	$AB \rightarrow AB \otimes A_pB_p$
Band 3	(−, 1)	$AE \rightarrow AEBC \rightarrow AEBC \otimes A_pB_p$
Band 4	(−, 0)	$AF \rightarrow AFBC \rightarrow AFBC \otimes A_pB_p$
Band 5	(−, 0)	(AG)
Band 6	(−, 1)	(AH)
Band 7	(−, 0)	(BE)
Band 8	(+, 0/1)	$E_pG_p/F_pG_p \rightarrow E_pG_p/F_pG_p \otimes AB \rightarrow E_pG_p/F_pG_p \otimes AB \otimes A_pB_p$
Band 9	(−, 1/0)	$A_pE_p/A_pF_p \rightarrow A_pE_p/A_pF_p \otimes AB \rightarrow A_pE_p/A_pF_p \otimes AB \otimes B_pC_p$
Band 10	(+, 0)	γ vibration
Band11	(+, 1)	γ vibration
Band 12	(+, 0)	(I_pA_pAB)
Band 13	(−, 0)	$(BEAD)$

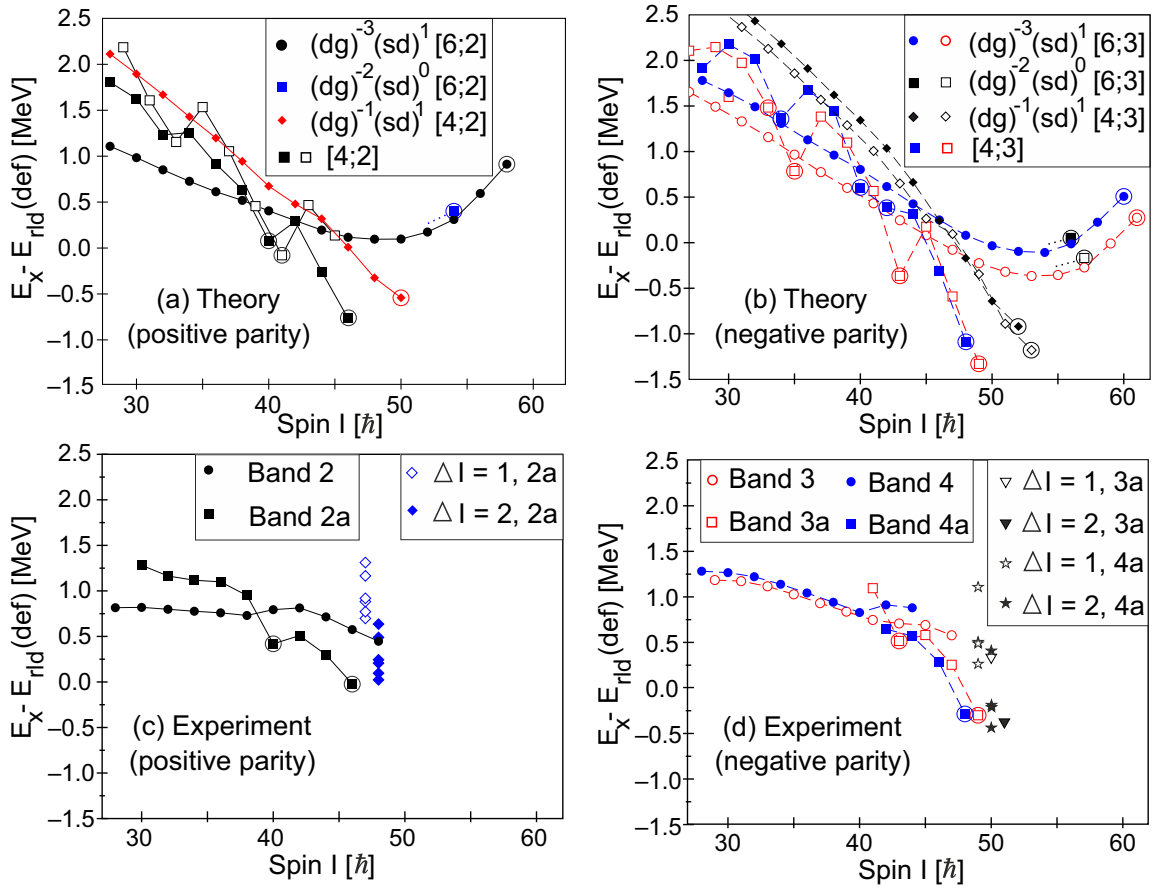

FIG. 26. Calculated excitation energy, minus a deformed rotating liquid-drop reference, plotted as a function of spin for (a) the predicted positive-parity states and (b) the predicted negative-parity in ^{158}Er. Full lines represent positive parity and dashed line negative parity. Closed symbols denote even spin, open symbols odd spin. Aligned oblate states are encircled. Configurations are labeled as described in the text, i.e., with the number of $h_{11/2}$ protons and $i_{13/2}$ neutrons $[p_1; n_3]$. Configurations with a constraint on the number of $(d_{5/2}g_{7/2})$ proton holes and $(s_{1/2}d_{3/2})$ protons in the $N_{\rm osc} = 4$ shell are indicated. The corresponding experimental energies are plotted for (c) bands 2 and 2a, and (d) bands 3, 3a, 4, and 4a. The transitions feeding the band-terminating states at 46^+, 48^-, and 49^- are included in (c) and (d) assuming they have dipole ($\Delta I = 1$) or quadrupole ($\Delta I = 2$) multipolarity.

higher spin can only be generated by particle-hole excitations across the $Z = 64$ or $N = 82$ shell gaps, leading to *core-excited* configurations.

For the states feeding the $I^\pi = 46^+$, 48^-, and 49^- terminating states, it is appropriate to consider proton particle-hole excitations across the $Z = 64$ shell gap. For instance, protons may be promoted from the $d_{5/2}g_{7/2}$ subshells below $Z = 64$ into the $h_{11/2}$ or $s_{1/2}d_{3/2}$ subshells above $Z = 64$, as discussed in Refs. [28,29,41,81,82]. New calculations are presented here, based on the cranked Nilsson-Strutinsky (CNS) method [70], with an updated set of Nilsson parameters. The methods introduced in Ref. [13] have also been employed, making it possible to compare experiment and theory on an absolute scale. Furthermore, for some configurations, these calculations introduce a constraint on the number of $(d_{5/2}g_{7/2})$ proton holes and the number of $(s_{1/2}d_{3/2})$ protons in the $N_{\rm osc} = 4$ shell. In the calculations, the configurations are labeled relative to a ^{146}Gd ($Z = 64$, $N = 82$) closed core, i.e.,

$$\pi(h_{11/2})^{p_1}(h_{9/2}f_{7/2})^{p_2}(i_{13/2})^{p_3}$$
$$\cdots \nu(N_{\rm osc} = 4)^{-n_1}(h_{11/2})^{-n_2}(i_{13/2})^{n_3},$$

specifying the number of particles and holes in orbitals outside the core. The configurations are given in the shorthand notation

$$[p_1(p_2p_3); (n_1n_2)n_3],$$

where the numbers in parentheses are only given when they are different from zero. Note that the number of $N_{\rm osc} = 4$ protons and the number of $(h_{9/2}, h_{11/2})$ neutrons are not labeled for simplicity unless they are constrained in the calculations.

The results are displayed in Fig. 26, where it can be seen that there is a good correspondence for those states that stand out as low lying in the experimental data at 40^+, 46^+, 43^-, 48^-, and 49^-. The measured 42^- state in band 4a is slightly favored, which is consistent with a calculated aligned state, in a similar fashion to the 40^+ and 43^- states in bands 2a and 3a, respectively. The calculations presented in Fig. 26(a) also predict a favored aligned 41^+ state with a similar configuration to the aligned 40^+ state, but with the six $(h_{9/2}, f_{7/2})$ neutrons coupled to $I = 13$ instead of $I = 12$. However, the $(+, 1)$ states in Fig. 26(a) have not been observed. The calculations also predict that, beyond the

favored terminations, no configuration stands out as particularly favored and that a large number of possible configurations compete [28].

Band 2 is assigned as the [6; 2] configuration, with the proton configuration most naturally understood as $\pi(d_{5/2}g_{7/2})^{-2}(h_{11/2})^{6}$ with a maximum spin of $I_{\max} = 6 + 18 = 24$, which leads to $I_{\max} = 54$ when combined with the $(i_{13/2})^{2}$, $(h_{9/2}f_{7/2})^{6}$ neutron configuration. The $\pi(d_{5/2}g_{7/2})^{-3}(h_{11/2})^{6}(s_{1/2})^{1}$ configuration is essentially degenerate with the former for $I \approx 50$ and even slightly favored at higher spins. This configuration has $I_{\max} = 28$ and thus $I_{\max} = 58$ for the full [6; 2] Configuration. This configuration is plotted in Fig. 26(a) and, for simplicity, the terminating state at $I_{\max} = 54$ is shown. The experimental continuation of band 2, after its crossing with band 2a, appears to drop in energy for $I > 42$ [see Fig. 26(c)], which suggests that it undergoes a band crossing. However, the drop in energy observed at spin $I > 42$ is not seen in the [6; 2] configurations. A possible interpretation is the configuration $\pi(h_{11/2})^{4}$ with one proton excited from the $(d_{5/2}g_{7/2})$ to the $(s_{1/2}d_{3/2})$ orbital. This is plotted in Fig. 26(a) and is the favored configuration up to $I = 50$. Several other calculated configurations also lie close in energy, for instance the $\pi(h_{11/2})^{5}\nu(i_{13/2})^{3}$ configuration. These other configurations are not plotted on the figure for simplicity. However, it seems unlikely that such a transition from a $\pi(h_{11/2})^{6}\nu(i_{13/2})^{2}$ to $\pi(h_{11/2})^{5}\nu(i_{13/2})^{3}$ configuration would lead to such a smooth transition as observed.

The calculations for negative parity follow closely the situation for positive parity. Bands 3 and 4 are the [6; 3] configuration. The $\pi(d_{5/2}g_{7/2})^{-3}(s_{1/2})^{1}$ [6; 3] configuration, plotted in Fig. 26(b), has an $I_{\max} = 60, 61$. The configurations $\pi(d_{5/2}g_{7/2})^{-2}(s_{1/2}d_{3/2})^{0}$ [6; 3] follow closely this configuration but have an $I_{\max} = 56, 57$, and these states are indicated in Fig. 26(b). For both negative-parity bands there is also an indication of a drop in energy at $\approx 42\hbar$; see Fig. 26(d). Similarly to the [6; 2] configuration, this is not predicted in the [6; 3] configurations. An explanation for the drop in energy could be the [4; 3] configuration with one proton excited from the $(d_{5/2}g_{7/2})$ to the $(s_{1/2}d_{3/2})$ orbital. The $\pi(h_{11/2})^{5}\nu(i_{13/2})^{2}$ configuration is calculated at a similar energy.

Several high-energy, low-intensity transitions feeding the terminating states at 46^{+}, 48^{-}, and 49^{-} have been identified. Some of these feeding transitions were previously suggested in Refs. [24,30]. Multipolarity assignments were not possible for these transitions. However, similar behavior is expected in ^{158}Er as established in ^{157}Er, where some of the transitions that feed the terminating states were measured to be either stretched dipole or stretched quadrupole in character [28,29]. The high-energy transitions feeding the band-terminating states at 46^{+}, 48^{-}, and 49^{-} in ^{158}Er are included in Figs. 26(c) and 26(d). They are drawn assuming both dipole ($\Delta I = 1$) and quadrupole ($\Delta I = 2$) character. Comparing with the calculations, it appears that the lower-energy feeders are more likely to be dipoles and the higher-energy feeders quadrupoles. A mixture of dipole and quadrupole feeders, as observed in ^{157}Er, is therefore likely.

The 1993 keV feeder of band 4a and the 1319 keV feeder of band 3a appear to connect to a level at an excitation energy of 20 122 keV (see Fig. 5). This level could be a 50^{-} core-excited state that feeds band 4a via an $E2$ transition (1993 keV) and band 3a via an $M1$ transition (1319 keV). The experimental intensity branching ratio for these decays implies a $B(M1)/B(E2)$ ratio in excess of 30 $(\mu_N/eb)^2$ (see Fig. 22 for context). This extremely large value can only occur for a severely hindered non-collective $E2$ transition from the new 50^{-} state into the oblate 48^{-} terminating state.

Another finding, consistent with the features seen in band 2 and 2a at high spin, was the observation in Ref. [21] of "fast" (band 2 continuation) and "slow" (band 2a) branches feeding the 38^{+} state; see Fig. 5. This is understood as the crossing of a near-prolate collective rotational structure by an energetically favored, weakly collective sequence that terminates into a noncollective oblate shape. This was deduced by comparing the spectra coincident with the 1058 keV transition in band 2, in both thin self-supporting target data, where the excited nuclei decay in flight, and thick target data, where the excited nuclei decay after stopping in the Au backing. A clear difference was observed with the 1202 and 1209 keV in the continuation of band 2 not being observed in the thick target data unlike the band 2a transitions of 827, 1280, 1030, and 971 keV which remained, see Fig. 1 of Ref. [21]. The "missing" 1202 and 1209 keV transitions were explained as being due to the fact that they are being emitted during the slowing down ($\approx$0.5 ps) process within the Au backing and thus constitute a "fast" branch being smeared out by Doppler shifts as the nucleus slows down and the variety of detector angles relative to the recoil direction. For the band 2a transitions to have good energy resolution they must constitute a "slow" branch having been emitted after an interval of $\geqslant 2$ ps [21]. These lifetime estimates included feeding times as well as the state lifetimes.

The present data confirm the work in Ref. [21], and extends it to higher spin in band 2. The same effect is also established in the negative-parity states of bands 3 and 4. Figure 27(a) is the equivalent of Fig. 1 in Ref. [21] showing a coincidence spectrum with the 1058 keV decay from the 38^{+} state in band 2. However, in order to produce as "clean" a spectrum as possible, the 1058 keV transition is in coincidence with all combinations of two lower spin transitions from 473 to 1017 keV in band 2; see Fig. 3. The "red" spectrum is from the thin target data and the "blue" spectrum from the thick target data. As initially observed in Ref. [21], there is a significant reduction in the intensity of the 1202 and 1209 keV transitions in the thick target data. However, in contrast, these transitions, albeit diminished, are still present indicating that while these transitions are "faster" than the band 2a transitions, these states must also have a "slow" feeding component. These transitions are however still present, albeit diminished, indicating that, while they are "faster" than the band 2a transitions, the terminating states must also have a "slow" feeding component. The reduction in intensity includes the 1141 keV and possibly 1151 keV transitions that extend band 2 to 46^{+}; see Fig. 5.

Figure 27 shows the corresponding overlapping thin target (red) and thick target (blue) spectra in coincidence with (b) the 1073 keV decay from the 41^{-} state in band 3 and (c) the 1026 keV decay from the 40^{-} state in band 4. In order to produce a clean spectrum, these transitions are in coincidence with all combinations of two lower spin transitions from 300

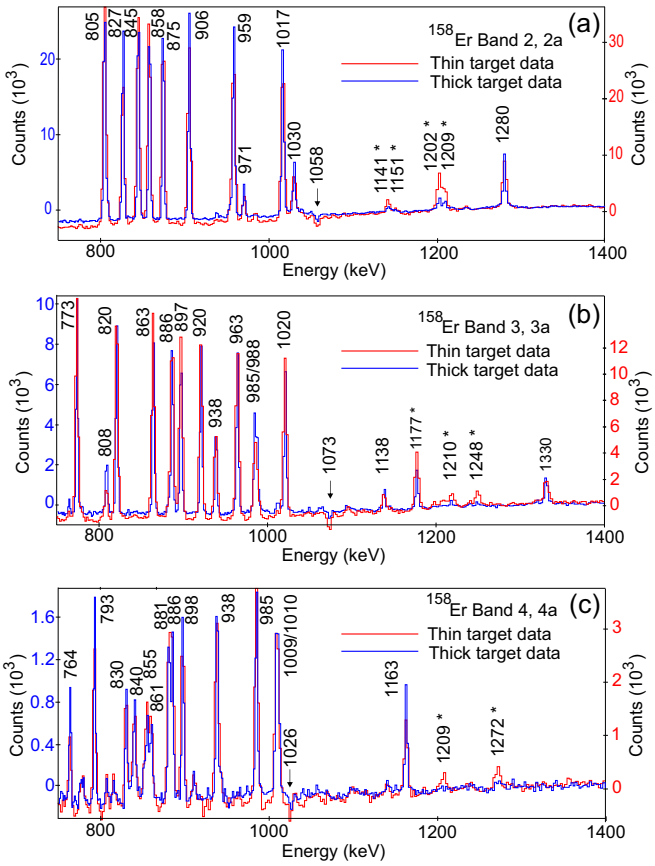

FIG. 27. Overlapping spectra from the thin-target (red) and thick-target (blue) datasets for (a) coincidences between all combinations of two lower spin transitions from 473 to 1017 keV, and the 1058 keV transition in band 2, (b) coincidences between all combinations of two lower spin transitions from 300 to 1020 keV, and the 1073 keV transition in band 3, and (c) coincidences between all combinations of two lower spin transitions from 236 to 985 keV, and the 1026 keV transition in band 4; see Fig. 5 and text for details. The 1058, 1073, and 1026 keV γ rays are indicated. Transitions in the "slow" feeding branches are labeled with an asterisk $*$.

to 1020 keV in band 3 and from 236 to 985 keV in band 4, respectively; see Fig. 5. The continuation of band 3 (the 1177, 1248, and 1210 keV transitions) and band 4 (the 1272 and 1209 keV transitions), show significantly reduced intensities compared with the transitions in bands 3a and 4a, respectively. This is consistent with "fast" and "slow" sequences in the collective and terminating branches, as observed in band 2. A summary of the "fast" and "slow" transitions in the band termination region is given in Table III.

E. Collective bands beyond band termination

Three weakly populated rotational structures, with high dynamic moments of inertia (Fig. 25) and large quadrupole moments have been observed, see Sec. III J and Figs. 5 and 6. Similar bands have now been established in neighboring nuclei (^{157}Er [15], ^{159,160}Er [76]). The feeding profile of the strongest band in ^{158}Er [15], TSD band 1, suggested that it extends over a spin range of $\approx$ 23–65 $\hbar$, marking a return

TABLE III. Summary of the "fast" and "slow" γ-ray transitions, above 38^+ in band 2, 41^- in band 3, and 40^- in band 4; see text and Fig. 27.

Band	E_γ (keV)	Lifetime	Band	E_γ (keV)	Lifetime
2a $\rightarrow$ 2	827	slow	3a $\rightarrow$ 3	985	slow
2a	1280	slow	3a	1330	slow
2a	1030	slow	3a	988	slow
2a	971	slow	3a	808	slow
2	1202	fast	3	1177	fast
2	1209	fast	3	1248	fast
2	1141	fast	3	1210	fast
2	1151	fast			
4a $\rightarrow$ 4	1009	slow			
4a	1163	slow			
4a	1010	slow			
4a	764	slow			
4	1272	fast			
4	1209	fast			

to collectivity up into the so-called "ultrahigh-spin regime" towards $\approx 70\hbar$.

It was proposed [15] that these bands correspond to *triaxial strongly deformed* (TSD) structures, based on the predictions of early cranking calculations of Bengtsson and Ragnarsson [25] and Dudek and Nazarewicz [26]. The transition quadrupole moments of the observed ultrahigh-spin sequences in ^{157,158}Er were measured confirming that they were all associated with strongly deformed shapes [31,32]; see the Appendix, Table V. These experimental measurements helped to trigger further theoretical studies of ^{158}Er, for example, Refs. [83–86].

The dynamic moments of inertia $\mathcal{J}^{(2)}$ for the three bands in ^{158}Er are included in Fig. 25, where they are compared with other high-spin rotational structures. These bands include the lowest-energy superdeformed band in ^{152}Dy, the lowest-energy triaxial strongly deformed band in ^{163}Lu [74,75] and ^{160}Er [76], and the normal deformed bands 8 $(-, 1)$ and 9 $(-, 1)$ in ^{158}Er. All bands in ^{158}Er show a gradually decreasing behavior with rotational frequency. This is similar to the lowest-energy superdeformed band in ^{152}Dy [72,73]. The similarities and differences between the variety of nuclear shapes and configurations can be seen in this figure.

The specific nature and deformation of the proposed "TSD" bands in this region is not straightforward and more theoretical studies, along with new experimental information, are required. Indeed, the theoretical investigation of Ref. [87] challenges previous interpretations and suggests that in the Lu isotopes the deformation of the TSD bands may not be very different from that of the normal-deformation bands.

Calculated potential-energy surfaces are shown in Fig. 28 for ^{158}Er at $I^\pi = 49^-, 59^-, 69^-$, and 79^-, where triaxial minima are labeled as $TSD1$, $TSD2$, and $TSD3$. Mean lifetime measurements have been performed for the proposed TSD bands in ^{157,158}Er [31,32] in order to distinguish between these triaxial shapes. While the results are consistent with enhanced quadrupole deformation, it was not possible to conclusively define the triaxial minimum. Indeed, the large experimental

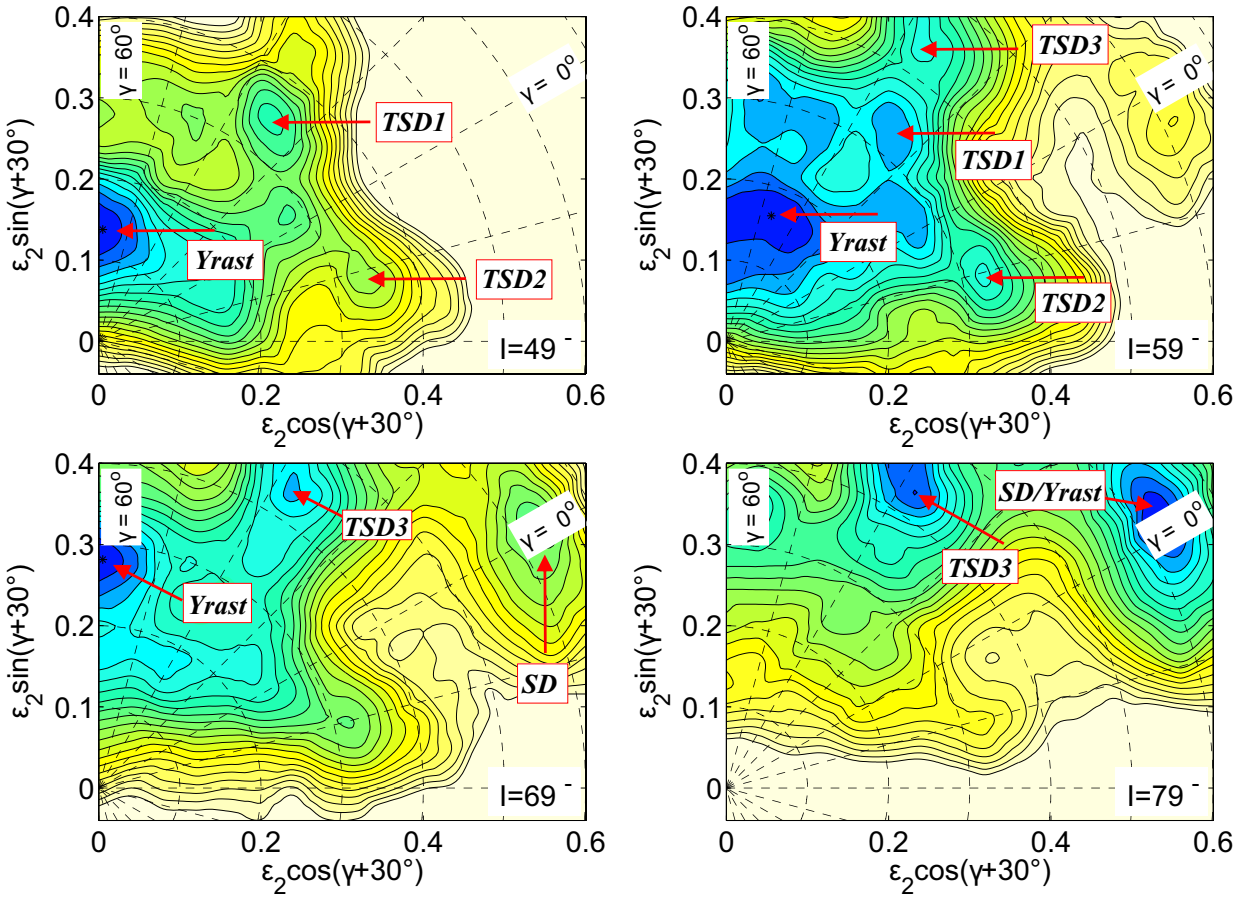

FIG. 28. Potential energy surface plots for $I^{\pi} = 49^{-}, 59^{-}, 69^{-}$ and 79^{-} in ^{158}Er. The triaxial minima discussed in [31,32] in comparing to the Q_t values are labeled $TSD1$, $TSD2$, and $TSD3$. The yrast and superdeformed (SD) minima are also indicated. The contour line separation is 0.25 MeV.

value of Q_t led to the conclusion that they could either be assigned to a negative-γ deformation, $\varepsilon_2 \approx 0.35$, $\gamma \approx -20^{\circ}$ ($TSD2$), or to a larger deformation with positive γ, $\varepsilon_2 \approx 0.43$, $\gamma \approx 25^{\circ}$ ($TSD3$) [31,32].

The deformed positive-γ minimum ($TSD3$) is well pronounced at high spin where experimentally the bands would be populated in the reaction. The same triaxial minima are also predicted in the calculations for ^{156}Er [41] and ^{160}Er [76]. Indeed, in ^{160}Er the equivalent $TSD3$ minimum is clearly preferred at the highest spins [76]. In addition, the TSD bands in ^{160}Er have a $\mathcal{J}^{(2)}$ similar to the bands in ^{158}Er; see Fig. 25. Experimentally the positive-γ minimum is the most probable for these bands, but the negative-γ minimum cannot be completely ruled out.

The present CNS calculations suggest that, in addition to proton particle-hole excitations, neutron particle-hole excitations are also needed to build the high-spin TSD structures. For negative-γ deformation, where the single-particle Routhians are published as Fig. 7 in Ref. [76], there is a large $Z = 66$ gap at low frequencies. However, for frequencies $\hbar\omega \approx 0.7$ MeV, both the lowest ($f_{7/2}/h_{9/2}$) and $i_{13/2}$ orbitals come down in energy leading to a gap for $Z = 68$ at $\hbar\omega \approx 0.8$ MeV. For the configuration with the orbitals below this gap filled, the dominating j-shells relative to $Z = 64$ core can be identified. With the labeling as specified in Sec. IV D, it is denoted by 6(11). For neutrons there is a small gap for $N = 91$ in a large frequency interval, with the configuration (22)5. Favored configurations for $N = 90$ are then formed by making a hole in one of the five orbitals below $N = 91$ and combining them with the proton configuration of the $Z = 68$ gap. In these calculations, the lowest energy configuration is [6(11); (22)4], where the hole is made in the $N_{\rm osc} = 6$ orbital. This configuration with odd spin is thus the favored assignment for TSD band 1 within the $\varepsilon_2 \approx 0.35$, $\gamma \approx -20^{\circ}$ minimum. The TSD band 2 might then be assigned to the odd spin configuration with the hole in the ($h_{9/2}$, $f_{7/2}$) orbitals instead, [6(11); (22)5]. The predicted configurations have spins consistent with the values in Fig. 6 and [15].

For the positive-γ shape, $TSD3$, with $\varepsilon_2 \approx 0.43$, $\gamma \approx 25^{\circ}$, the configurations involve the same orbitals as for negative γ except that for neutrons there is the possibility of populating the $N_{\rm osc} = 6$ $i_{11/2}$, $g_{9/2}$ orbitals, in addition to the $N_{\rm osc} = 7$ $j_{15/2}$ intruder orbital. Thus a typical feature of these larger deformation triaxial configurations is the presence of four $N_{\rm osc} = 4$ neutron holes and one neutron excited to the $N_{\rm osc} = 7$ shell.

An issue with the comparison with experiment in the $TSD3$ minimum is that the calculations require the spin values to be

increased by 3–4 $\hbar$ with an associated increase in excitation energy compared with the tentative assignments made by Paul *et al.* [15], shown in Fig. 6. This increase in spin is the same conclusion as that presented in Ref. [86], where the authors prefer to assign the $\pi 6^2 \nu 7^1$ configuration to be associated with the minimum at $\varepsilon_2 \approx 0.43$, $\gamma \approx 10$–15°. They noted that *"If the theoretical spin assignments ...turned out to be correct, the experimental band 1 in* ^{158}Er *would be the highest-spin structure ever observed. The current study stresses the need for more precise measurements of* Q_t *and reliable estimates of spins in these bands."* Observing such high spin states is then not so far from the fission limit expected for a nucleus of this mass.

The calculations for positive and negative γ deformation have suggestions for the nature of TSD band 3. However, there are hints from the coincidence data that the lower-energy transitions of TSD band 1 are present, implying TSD band 3 decays into TSD band 1. Unfortunately, these observations are not reproducible with sufficient confidence to establish this connection. However, this possibility, together with the fact that the dynamic moments of inertia of TSD band 3 and TSD band 1 are so similar (see Fig. 25 and Ref. [32]), would be consistent with TSD band 3 being a wobbling excitation based on TSD band 1, as observed in ^{163}Lu [74].

V. SUMMARY AND CONCLUSIONS

High-spin experiments using the Gammasphere spectrometer, with both thin (self-supporting) and thick (backed) targets, have been performed in order to study the level structure of ^{158}Er. More than 200 new transitions and six new rotational bands have been observed. Angular-intensity ratio information has been used for spin and parity assignments. Two strongly coupled rotational bands have been identified as two-quasiproton excitations, based on their measured $B(M1)/B(E2)$ ratios of reduced transition probabilities, along with the observed characteristic neutron and proton alignment properties and comparisons with neighboring nuclei. The high-spin states near band termination have been discussed using cranked Nilsson-Strutinsky calculations. Assignments are made for the terminating structures and continuing collective sequences including the non-collective oblate states at 40^+, 42^-, 43^-, 46^+, 48^-, and 49^-. Two lifetime branches in the positive parity states above 38^+, consistent with the crossing of a near-prolate collective "fast" rotational structure by an energetically favored weakly collective "slow" structure that terminates in a non-collective oblate shape are confirmed, and the fast branch is extended to higher spin. Two lifetime branches are also established in the negative-parity states above 40^- and 41^-. The fully aligned band-terminating states at 46^+, 48^-, and 49^- are fed by many weak transitions in the energy range 1200–2100 keV. These feeding transitions originate mainly from weakly deformed configurations involving core-breaking proton particle-hole excitations across the $Z = 64$ semimagic shell gap, as observed in the neighboring nuclei, for example ^{156}Er and ^{157}Er. At higher spin values, three collective rotational structures, which are most probably associated with triaxial strongly deformed shapes, have been established. These sequences extend up to spin $\approx$65–70 $\hbar$, adding to the wide variety of nuclear structure phenomena observed in this rare-earth nucleus. The observation of these sequences raises multiple questions pointing to the need for further experimental investigations, in particular, to firmly establish their spins and excitation energies. In addition, it would be interesting to observe further sequences in each of the predicted TSD minima and, even in the superdeformed minimum, in order to completely explore the full spectrum of shape coexistence expected in ^{158}Er at the highest possible spins. These questions, and many others may be answered by the next generation 4π γ-ray tracking spectrometers GRETA [88] and AGATA [89].

Data access statement: Data supporting this paper are included in the Appendix.

ACKNOWLEDGMENTS

The authors thank the operations staff of Gammasphere both at LBNL and ANL, and gratefully acknowledge the efforts of John Greene and Paul Morrall for their target preparation. We thank D. C. Radford for his RADWARE software package. This work has been supported in part by the United Kingdom Science and Technology Facilities Council under Grants No. ST/P004598/1, No. ST/V001027/1, and No. PP/F000677/1, by the U.S. National Science Foundation under Grants No. PHY-0756474 (FSU), No. PHY-0554762 (USNA), and No. PHY-0754674 (UND), by the U.S. Department of Energy, Office of Nuclear Physics under Contracts No. DE-AC02-06CH11357 (ANL), No. DE-FG02-94ER40834 (UMD), No. DE-AC02-05CH11231 (LBNL), No. DE-FG02-97ER41041 (UNC), No. DE-FG02-97ER41033(TUNL), and No. DE-FG02-96ER40983 (UTK), and by the State of Florida.

APPENDIX: EXPERIMENTAL RESULTS

The experimental results are presented in the Appendix, Tables IV and V.

Table IV lists excitation energies E_x, transition energies E_γ, relative intensities $I_\gamma^{\text{rel.}}$, angular intensity ratio R, multipolarity, and spin-parity assignments for the transitions observed in ^{158}Er. The multipolarity is indicated where an R value was measured in this work. Spin and parity assignments are taken from this work and [20] and references therein. The γ-ray energies are estimated to be accurate to ± 0.3 keV for the strong transitions ($I_\gamma^{\text{rel.}} > 10$), rising to ± 1.0 keV for the weaker transitions. The intensity measurements have been normalized to the 192.2 keV ($2^+ \rightarrow 0^+$) yrast transition with a value of 100. Errors on the intensities are estimated to be 5% of the quoted values for strong transitions ($I_\gamma^{\text{rel.}} > 10$) and 10% for the weaker transitions. Quantities in parentheses are tentative.

Table V lists measured transition quadrupole moments along with γ-ray energies (keV) in the TSD bands in ^{158}Er, Refs. [12,15,31,32]. The γ-ray energies are estimated to be accurate to ± 1.0 keV.

TABLE IV. Experimental properties for bands 1–13.

E_x (keV)	E_γ (keV)	$I_\gamma^{\text{rel.}}$	R	Multipolarity	$I^\pi_{\text{initial}} \rightarrow I^\pi_{\text{final}}$	Band
Band 1						
192.2	192.2	100.0	0.55(4)	$E2$	$2^+ \rightarrow 0^+$	1
527.2	335.0	100.0	0.72(4)	$E2$	$4^+ \rightarrow 2^+$	1
970.2	443.0	96.0	0.86(4)	$E2$	$6^+ \rightarrow 4^+$	1
1493.1	522.9	94.0	0.97(4)	$E2$	$8^+ \rightarrow 6^+$	1
1852.4	882.2	< 1.0			$\rightarrow 6^+$	$\rightarrow 1$
2027.0	1056.9	2.8			$(7^-) \rightarrow 6^+$	Level $(7^-) \rightarrow 1$
2072.0	578.9	82.0	0.96(4)	$E2$	$10^+ \rightarrow 8^+$	1
2680.1	608.1	66.0	0.94(4)	$E2$	$12^+ \rightarrow 10^+$	1
3373.1	492.9	0.6			$14^+ \rightarrow 12^+$	$1 \rightarrow 2$
3373.1	693.0	8.0	1.07(7)	$E2$	$14^+ \rightarrow 12^+$	1
4024.2	651.1	5.0	1.03(5)	$E2$	$16^+ \rightarrow 14^+$	1
4677.8	653.5	3.5			$18^+ \rightarrow 16^+$	1
5325.6	647.8	3.1	1.01(6)	$E2$	$20^+ \rightarrow 18^+$	1
5325.6	1097.1	0.6			$20^+ \rightarrow 18^+$	$1 \rightarrow 2$
6022.5	696.9	2.6	1.03(8)	$E2$	$22^+ \rightarrow 20^+$	1
6022.5	1135.5	0.3			$22^+ \rightarrow 20^+$	$1 \rightarrow 2$
6791.8	769.3	2.8	0.97(6)	$E2$	$24^+ \rightarrow 22^+$	1
6791.8	1165.1	0.3			$24^+ \rightarrow 22^+$	$1 \rightarrow 2$
7632.1	840.3	2.6	0.97(8)	$E2$	$26^+ \rightarrow 24^+$	1
7632.1	1200.9	0.2			$26^+ \rightarrow 24^+$	$1 \rightarrow 2$
8545.6	913.5	2.2	1.00(13)	$E2$	$28^+ \rightarrow 26^+$	1
8545.6	1269.5	0.1			$28^+ \rightarrow 26^+$	$1 \rightarrow 2$
9530.4	984.8	0.9			$(30^+) \rightarrow 28^+$	1
10381.9	834.4	0.1			$(32^+) \rightarrow (30^+)$	$1 \rightarrow 1a$
10381.9	851.5	0.4			$(32^+) \rightarrow (30^+)$	1
11325.1	943.2	0.45			$(34^+) \rightarrow (32^+)$	1
12338.8	1013.7	0.55			$(36^+) \rightarrow (34^+)$	1
13404.4	1065.6	0.4			$(38^+) \rightarrow (36^+)$	1
(14534.9)	(1130.5)	0.1			$(40^+) \rightarrow (38^+)$	1
Band 1a						
9547.2	1001.6	0.7			$(30^+) \rightarrow 28^+$	$1a \rightarrow 1$
10577.8	1030.5	0.3			$(32^+) \rightarrow (30^+)$	1a
10577.8	1047.6	0.2			$(32^+) \rightarrow (30^+)$	$1a \rightarrow 1$
11670.3	1092.5	0.2			$(34^+) \rightarrow (32^+)$	1a
(12799.1)	(1128.9)	0.1			$(36^+) \rightarrow (34^+)$	1a
Band 2						
2880.4	200.3	1.95			$12^+ \rightarrow 12^+$	$2 \rightarrow 1$
2880.4	393.7	0.8			$12^+ \rightarrow (10^+)$	$2 \rightarrow 10$
2880.4	808.3	5.7			$12^+ \rightarrow 10^+$	$2 \rightarrow 1$
3189.7	309.3	3.6	0.95(6)	E2	$14^+ \rightarrow 12^+$	2
3189.7	509.6	57.0	0.85(11)	E2	$14^+ \rightarrow 12^+$	$2 \rightarrow 1$
3662.2	472.5	50.0	0.92(4)	E2	$16^+ \rightarrow 14^+$	2
4228.3	566.1	46.0	0.92(4)	E2	$18^+ \rightarrow 16^+$	2
4886.6	658.3	40.0	0.97(4)	E2	$20^+ \rightarrow 18^+$	2
5626.8	740.2	35.1	0.94(4)	E2	$22^+ \rightarrow 20^+$	2
6431.7	804.9	31.3	0.93(4)	E2	$24^+ \rightarrow 22^+$	2
7276.6	844.9	24.5	0.92(4)	E2	$26^+ \rightarrow 24^+$	2
8134.8	858.2	22.2	1.02(4)	E2	$28^+ \rightarrow 26^+$	2
9009.6	874.8	18.0	0.97(4)	E2	$30^+ \rightarrow 28^+$	2
9915.2	905.6	14.1	0.93(4)	E2	$32^+ \rightarrow 30^+$	2
10873.9	958.7	13.5	0.95(4)	$E2$	$34^+ \rightarrow 32^+$	2
11890.6	1016.7	8.7	0.98(4)	$E2$	$36^+ \rightarrow 34^+$	2
12948.7	1058.1	7.6	1.00(5)	$E2$	$38^+ \rightarrow 36^+$	2
14151.1	983.1	0.5			$40^+ \rightarrow 38^+$	$2 \rightarrow 2a$
14151.1	1202.4	2.0	0.98(8)	$E2$	$40^+ \rightarrow 38^+$	2
15360.4	1209.3	1.0	1.01(12)	$E2$	$42^+ \rightarrow 40^+$	2

TABLE IV. *(Continued.)*

E_x (keV)	E_γ (keV)	$I_\gamma^{\text{rel.}}$	R	Multipolarity	$I^\pi_{\text{initial}} \rightarrow I^\pi_{\text{final}}$	Band
16501.7	1141.3	0.7			$44^+ \rightarrow 42^+$	2
17652.3	1150.6	0.3			$46^+ \rightarrow 44^+$	2
(18862.8)	(1210.5)	0.1	1.01(13)	$E2$	$(48^+) \rightarrow 46^+$	2
Band 2a						
9472.7	1338.2	0.8			$30^+ \rightarrow 28^+$	2a $\rightarrow$ 2
10280.1	807.4	2.0			$32^+ \rightarrow 30^+$	2a
10280.1	1270.5	0.8			$32^+ \rightarrow 30^+$	2a $\rightarrow$ 2
11214.8	934.7	1.0			$34^+ \rightarrow 32^+$	2a
11214.8	1299.5	0.5			$34^+ \rightarrow 32^+$	2a $\rightarrow$ 2
12230.5	1015.7	1.8			$36^+ \rightarrow 34^+$	2a
12230.5	1357.2	0.3			$36^+ \rightarrow 34^+$	2a $\rightarrow$ 2
13167.9	937.4	1.0			$38^+ \rightarrow 36^+$	2a
13167.9	1276.9	1.0			$38^+ \rightarrow 36^+$	2a $\rightarrow$ 2
13775.9	608.0	3.0			$40^+ \rightarrow 38^+$	2a
13775.9	827.2	4.0	1.08(5)	$E2$	$40^+ \rightarrow 38^+$	2a $\rightarrow$ 2
15056.0	1280.1	3.2	0.97(6)	$E2$	$42^+ \rightarrow 40^+$	2a
16086.3	1030.3	1.8	1.03(7)	$E2$	$44^+ \rightarrow 42^+$	2a
17057.2	970.9	1.55	1.01(14)	$E2$	$46^+ \rightarrow 44^+$	2a
17738.7	1652.4	0.07			$\rightarrow 44^+$	2a
18438.4	1381.2	0.08			$\rightarrow 46^+$	2a
18511.9	1454.7	0.08			$\rightarrow 46^+$	2a
(18599.3)	(1542.1)	<0.08			$\rightarrow 46^+$	2a
18622.7	1565.5	0.08			$\rightarrow 46^+$	2a
18659.3	1602.1	0.07			$\rightarrow 46^+$	2a
(18714.7)	(1657.5)	<0.08			$\rightarrow 46^+$	2a
(18807.5)	(1750.3)	<0.08			$\rightarrow 46^+$	2a
18905.2	1848.0	0.07			$\rightarrow 46^+$	2a
(18955.7)	(1898.5)	<0.08			$\rightarrow 46^+$	2a
19051.3	1994.1	0.07			$\rightarrow 46^+$	2a
Band 3						
2431.0	159.3	0.3			$9^- \rightarrow 9^-$	3 $\rightarrow$ 6
2431.0	359.1	0.7			$9^- \rightarrow 10^+$	3 $\rightarrow$ 1
2431.0	413.1	2.4	0.62(5)	$E1$	$9^- \rightarrow (8^+)$	3 $\rightarrow$ 10
2431.0	579.1	1.7	0.57(5)	$E1$	$9^- \rightarrow$	3 $\rightarrow$
2431.0	937.9	11.5	0.57(5)	$E1$	$9^- \rightarrow 8^+$	3 $\rightarrow$ 1
2730.9	244.5	0.7			$11^- \rightarrow (10^+)$	3 $\rightarrow$ 10
2730.9	299.9	9.7	0.89(4)	$E2$	$11^- \rightarrow 9^-$	3
2730.9	659.5	4.5	0.64(5)	$E1$	$11^- \rightarrow 10^+$	3 $\rightarrow$ 1
3154.5	423.6	13.8	0.92(4)	$E2$	$13^- \rightarrow 11^-$	3
3154.5	474.4	0.8			$13^- \rightarrow 12^+$	3 $\rightarrow$ 1
3695.1	540.6	12.3	0.98(4)	$E2$	$15^- \rightarrow 13^-$	3
4329.1	634.0	11.6	1.01(4)	$E2$	$17^- \rightarrow 15^-$	3
5021.5	692.4	11.5	0.96(4)	$E2$	$19^- \rightarrow 17^-$	3
5738.7	717.2	9.2	1.04(4)	$E2$	$21^- \rightarrow 19^-$	3
6476.3	737.6	8.4	1.02(4)	$E2$	$23^- \rightarrow 21^-$	3
7249.7	773.4	7.0	1.02(4)	$E2$	$25^- \rightarrow 23^-$	3
8069.7	820.0	6.0	0.98(4)	$E2$	$27^- \rightarrow 25^-$	3
8933.0	863.3	5.0	1.03(4)	$E2$	$29^- \rightarrow 27^-$	3
9819.4	886.4	4.2	0.98(4)	$E2$	$31^- \rightarrow 29^-$	3
10715.9	896.5	4.1	0.98(4)	$E2$	$33^- \rightarrow 31^-$	3
11635.9	920.0	3.3	1.05(5)	$E2$	$35^- \rightarrow 33^-$	3
12599.2	963.3	3.2	0.96(5)	$E2$	$37^- \rightarrow 35^-$	3
13618.9	1019.7	2.8	1.05(6)	$E2$	$39^- \rightarrow 37^-$	3
14691.8	1072.9	2.0	1.08(7)	$E2$	$41^- \rightarrow 39^-$	3
15868.4	1176.6	0.75	1.17(11)	$E2$	$43^- \rightarrow 41^-$	3
17116.8	1248.4	0.2			$45^- \rightarrow 43^-$	3
17116.8	1439.5	0.1			$45^- \rightarrow 43^-$	3 $\rightarrow$ 3a

TABLE IV. *(Continued.)*

E_x (keV)	E_γ (keV)	$I_\gamma^{\text{rel.}}$	R	Multipolarity	$I^\pi_{\text{initial}} \rightarrow I^\pi_{\text{final}}$	Band
18326.9	1210.1	0.1			$47^- \rightarrow 45^-$	3
Band 3a						
15040.9	1422.0	<0.1			$(41^-) \rightarrow 39^-$	3a → 3
15676.8	(635.9)				$43^- \rightarrow (41^-)$	3a
15676.8	985.0	0.85	0.98(7)	$E2$	$43^- \rightarrow 41^-$	3a → 3
17006.9	1137.8	0.25			$45^- \rightarrow 43^-$	3a → 3
17006.9	1330.1	0.4	0.98(23)	$E2$	$45^- \rightarrow 43^-$	3a
17994.8	937.6	<0.1			$47^- \rightarrow 46^+$	3a → 2a
17994.8	987.9	0.5	0.98(7)	$E2$	$47^- \rightarrow 45^-$	3a
18803.1	808.3	0.5	0.95(13)	$E2$	$49^- \rightarrow 47^-$	3a
20122.3	1319.2	0.1			$(50^-) \rightarrow 49^-$	3a
Band 4						
2333.4	306.4	0.3			$8^- \rightarrow (7^-)$	4 → Level (7^-)
2333.4	420.6	2.2			$8^- \rightarrow (7^+)$	4 → 11
2333.4	480.9	0.4			$8^- \rightarrow$	4 →
2333.4	840.3	3.4			$8^- \rightarrow 8^+$	4 → 1
2569.8	138.6	0.45			$10^- \rightarrow 9^-$	4 → 3
2569.8	236.4	7.0	0.91(6)	$E2$	$10^- \rightarrow 8^-$	4
2569.8	297.4	0.45			$10^- \rightarrow 9^-$	4 → 6
2569.8	497.4	1.8			$10^- \rightarrow 10^+$	4 → 1
2569.8	115.5	1.0			$10^- \rightarrow (9^+)$	4 → 11
2954.9	223.7	0.9			$12^- \rightarrow 11^-$	4 → 3
2954.9	385.1	8.2	0.98(6)	$E2$	$12^- \rightarrow 10^-$	4
3474.1	319.3	0.2			$14^- \rightarrow 13^-$	4 → 3
3474.1	519.2	8.7	1.03(6)	$E2$	$14^- \rightarrow 12^-$	4
4102.9	407.6	0.1			$16^- \rightarrow 15^-$	4 → 3
4102.9	628.8	7.8	0.99(6)	$E2$	$16^- \rightarrow 14^-$	4
4812.3	483.6	0.2			$18^- \rightarrow 17^-$	4 → 3
4812.3	709.4	7.2	1.02(6)	$E2$	$18^- \rightarrow 16^-$	4
5538.1	725.8	7.0	1.02(5)	$E2$	$20^- \rightarrow 18^-$	4
6219.9	681.8	4.2	1.02(8)	$E2$	$22^- \rightarrow 20^-$	4
6947.8	727.9	3.0	1.03(5)	$E2$	$24^- \rightarrow 22^-$	4
7740.3	792.5	2.9	0.95(8)	$E2$	$26^- \rightarrow 24^-$	4
8601.2	839.4	0.85			$28^- \rightarrow 26^-$	4 → 9
8601.2	860.9	1.1	0.98(13)	$E2$	$28^- \rightarrow 26^-$	4
9456.3	855.1	0.9	1.03(15)	$E2$	$30^- \rightarrow 28^-$	4
9456.3	885.6	3.0	1.04(13)	$E2$	$30^- \rightarrow 28^-$	4 → 9
10337.7	881.4	4.4	0.91(9)	$E2$	$32^- \rightarrow 30^-$	4
11235.7	898.0	2.5	0.96(9)	$E2$	$34^- \rightarrow 32^-$	4
12174.0	938.3	2.4	0.89(7)	$E2$	$36^- \rightarrow 34^-$	4
13159.2	985.2	1.9	1.01(9)	$E2$	$38^- \rightarrow 36^-$	4
14184.7	1025.5	1.5	0.95(5)	$E2$	$40^- \rightarrow 38^-$	4
15457.1	1272.4	0.5			$42^- \rightarrow 40^-$	4
16665.7	1208.6	0.2			$44^- \rightarrow 42^-$	4
16665.7	1472.5	0.1			$44^- \rightarrow 42^-$	4 → 4a
Band 4a						
15194.0	1009.3	0.9	0.94(9)	$E2$	$42^- \rightarrow 40^-$	4a → 4
16356.8	1162.8	0.6	0.94(23)	$E2$	$44^- \rightarrow 42^-$	4a
17366.5	1009.7	0.5	0.94(9)	$E2$	$46^- \rightarrow 44^-$	4a
18130.4	763.9	0.45			$48^- \rightarrow 46^-$	4a
19366.8	1236.4	0.05			$\rightarrow 48^-$	4a
19590.1	1459.7	0.05			$\rightarrow 48^-$	4a
19607.7	1477.3	0.05			$\rightarrow 48^-$	4a
(19659.3)	(1528.9)	<0.03			$\rightarrow 48^-$	4a
(19724.5)	(1594.1)	<0.03			$\rightarrow 48^-$	4a
(19743.6)	(1613.2)	<0.03			$\rightarrow 48^-$	4a
(19767.1)	(1636.7)	<0.03			$\rightarrow 48^-$	4a

TABLE IV. *(Continued.)*

E_x (keV)	E_γ (keV)	$I_\gamma^{\text{rel.}}$	R	Multipolarity	$I^\pi_{\text{initial}} \rightarrow I^\pi_{\text{final}}$	Band
(19779.2)	(1648.8)	<0.03			$\rightarrow 48^-$	4a
(20123.7)	(1993.3)	<0.03			$(50^-) \rightarrow 48^-$	4a
20211.0	2080.6	0.03			$\rightarrow 48^-$	4a
Band 5						
2888.2	333.6	0.1			$(8^-) \rightarrow (8^-)$	$5 \rightarrow 9$
3004.6	450.0	0.1			$(9^-) \rightarrow (8^-)$	$5 \rightarrow 9$
3004.6	220.0	0.1			$(9^-) \rightarrow (9^-)$	$5 \rightarrow 9$
3205.0	200.1	0.5			$(10^-) \rightarrow (9^-)$	$5 \rightarrow 9$
3205.0	316.8	0.5			$(10^-) \rightarrow (8^-)$	5
3205.6	421.1	0.5			$(10^-) \rightarrow (9^-)$	$5 \rightarrow 9$
3676.7	471.7	0.5			$(12^-) \rightarrow (10^-)$	$5 \rightarrow 9$
4244.0	567.3	0.6			$(14^-) \rightarrow (12^-)$	5
4886.0	642.0	0.35			$(16^-) \rightarrow (14^-)$	5
5578.0	692.0	0.25			$(18^-) \rightarrow (16^-)$	5
6305	727.0	0.2			$(20^-) \rightarrow (18^-)$	5
7048.2	743.2	0.1			$(22^-) \rightarrow (20^-)$	5
7822.2	774.0	<0.1			$(24^-) \rightarrow (22^-)$	5
8655.5	833.0	<0.1			$(26^-) \rightarrow (24^-)$	5
9553.6	898.4	<0.1			$(28^-) \rightarrow (26^-)$	5
10506.0	952.4	<0.1			$(30^-) \rightarrow (28^-)$	5
Band 6						
2272.4	779.3	2.6			$9^- \rightarrow 8^+$	$6 \rightarrow 1$
2760.1	487.4	1.0			$11^- \rightarrow 9^-$	6
2760.1	687.9	2.4			$11^- \rightarrow 10^+$	$6 \rightarrow 1$
3303.7	543.6	1.5			$(13^-) \rightarrow 11^-$	6
3303.7	623.2	1.1			$(13^-) \rightarrow 12^+$	$6 \rightarrow 1$
3906.0	602.3	1.5			$(15^-) \rightarrow (13^-)$	6
4569.4	663.4	1.4			$(17^-) \rightarrow (15^-)$	6
5293.6	724.2	0.8			$(19^-) \rightarrow (17^-)$	6
6063.5	769.9	0.3			$(21^-) \rightarrow (19^-)$	6
6869.0	805.5	0.1			$(23^-) \rightarrow (21^-)$	6
Band 7						
3516.5	362.0				$(12^-) \rightarrow 13^-$	$7 \rightarrow 3$
3516.5	786.2				$(12^-) \rightarrow 11^-$	$7 \rightarrow 3$
4015.1	498.6				$(14^-) \rightarrow (12^-)$	7
4015.1	1060.5				$(14^-) \rightarrow 12^-$	$7 \rightarrow 4$
4556.9	541.8				$(16^-) \rightarrow (14^-)$	7
4556.9	1083.1				$(16^-) \rightarrow 14^-$	$7 \rightarrow 4$
5159.8	602.9				$(18^-) \rightarrow (16^-)$	7
5819.7	252.4		0.66(9)	$M1/E2$	$20^- \rightarrow 19^-$	$7 \rightarrow 9$
5819.7	659.9				$20^- \rightarrow (18^-)$	7
Band 8						
(4602.8)					(15^+)	8
(4889.6)	286.8				$(16^+) \rightarrow (15^+)$	8
(5122.2)	232.6	1.0			$(17^+) \rightarrow (16^+)$	8
(5122.2)	519.4				$(17^+) \rightarrow (15^+)$	8
(5362.9)	241.6	0.15			$(18^+) \rightarrow (17^+)$	8
(5362.9)	474.1				$(18^+) \rightarrow (16^+)$	8
(5617.5)	254.5	0.6			$(19^+) \rightarrow (18^+)$	8
(5617.5)	495.4	0.25			$(19^+) \rightarrow (17^+)$	8
(5617.5)	(1389.4)	0.15			$(19^+) \rightarrow 18^+$	$8 \rightarrow 2$
(5885.7)	269.2	0.1			$(20^+) \rightarrow (19^+)$	Level $(20^+) \rightarrow 8$
(5885.7)	(999.1)				$(20^+) \rightarrow 20^+$	Level $(20^+) \rightarrow 2$
(5896.8)	279.3	0.2			$(20^+) \rightarrow (19^+)$	8
(5896.8)	533.9	0.2			$(20^+) \rightarrow (18^+)$	8
(5896.8)	(1668.5)	0.05			$(20^+) \rightarrow 18^+$	$8 \rightarrow 2$
(6184.3)	288.6	0.5			$(21^+) \rightarrow (20^+)$	8

TABLE IV. *(Continued.)*

E_x (keV)	E_γ (keV)	$I_\gamma^{\text{rel.}}$	R	Multipolarity	$I^\pi_{\text{initial}} \to I^\pi_{\text{final}}$	Band
(6184.3)	298.9	0.1			$(21^+) \to (20^+)$	$8 \to$ Level (20^+)
(6184.3)	567.4				$(21^+) \to (19^+)$	8
(6496.2)	310.8	0.6	0.60(15)	$M1/E2$	$(22^+) \to (21^+)$	8
(6496.2)	599.4	0.5			$(22^+) \to (20^+)$	8
(6824.0)	329.1	0.9			$(23^+) \to (22^+)$	8
(6824.0)	639.7	0.8			$(23^+) \to (21^+)$	8
(7170.8)	345.6	1.5	0.64(8)	$M1/E2$	$(24^+) \to (23^+)$	8
(7170.8)	674.7	1.0			$(24^+) \to (22^+)$	8
(7530.8)	361.8	1.2	0.48(13)	$M1/E2$	$(25^+) \to (24^+)$	8
(7530.8)	707.3	0.9			$(25^+) \to (23^+)$	8
(7908.6)	376.5	0.95			$(26^+) \to (25^+)$	8
(7908.6)	738.2	0.8			$(26^+) \to (24^+)$	8
(8298.1)	391.6	0.9			$(27^+) \to (26^+)$	8
(8298.1)	767.8	0.7			$(27^+) \to (25^+)$	8
(8704.8)	405.5	0.8			$(28^+) \to (27^+)$	8
(8704.8)	797.0	0.7			$(28^+) \to (26^+)$	8
(9123.6)	420.6	0.8			$(29^+) \to (28^+)$	8
(9123.6)	825.5	0.8			$(29+) \to (27^+)$	8
(9555.1)	430.1	0.6			$(30^+) \to (29^+)$	8
(9555.1)	850.9	0.6			$(30^+) \to (28^+)$	8
(9997.7)	443.1				$(31^+) \to (30^+)$	8
(9997.7)	874.1	0.8			$(31^+) \to (29^+)$	8
(10451.0)	452.0	0.45			$(32^+) \to (31^+)$	8
(10451.0)	895.9	0.5			$(32^+) \to (30^+)$	8
(10925.2)	475.9				$(33^+) \to (32^+)$	8
(10925.2)	927.3	0.5			$(33^+) \to (31^+)$	8
(11406.4)	(480.4)				$(34^+) \to (33^+)$	8
(11406.4)	956.4	0.5			$(34^+) \to (32^+)$	8
(11910.6)	985.0	0.55			$(35^+) \to (33^+)$	8
(12420.9)	1015.1	0.4			$(36^+) \to (34^+)$	8
(12952.0)	1041.2	0.6			$(37^+) \to (35^+)$	8
(13488.3)	1067.1	0.45			$(38^+) \to (36^+)$	8
(14037.5)	(1085.2)	0.1			$(39^+) \to (37^+)$	8
(14608.8)	(1121.1)	0.1			$(40^+) \to (38^+)$	8
Band 9						
1614.5	571.1				$(3^-) \to 3^+$	$9 \to 11$
1614.5	794.6				$(3^-) \to 2^+$	$9 \to 11$
2050.2	435.4				$(5^-) \to (3^-)$	9
2050.2	611.5				$(5^-) \to 5^+$	$9 \to 11$
2050.2	865.4				$(5^-) \to (4^+)$	$9 \to 11$
2131.8	1161.6				$6^- \to 6^+$	$9 \to 1$
2401.5	351.3				$7^- \to (5^-)$	9
2401.5	269.5		0.63(6)	$M1/E2$	$7^- \to 6^-$	9
2401.5	1430.9				$7^- \to 6^+$	$9 \to 1$
2554.6	153.1	0.8			$8^- \to 7^-$	9
2554.6	422.0	1.7			$8^- \to 6^-$	9
2784.0	229.4	0.4	0.69(6)	$M1/E2$	$9^- \to 8^-$	9
2784.0	382.4	3.9			$9^- \to 7^-$	9
2984.1	200.0	1.1	0.72(12)	$M1/E2$	$10^- \to 9^-$	9
2984.1	429.5	2.5			$10^- \to 8^-$	9
3256.3	272.4		0.63(6)	$M1/E2$	$11^- \to 10^-$	9
3256.3	472.4				$11^- \to 9^-$	9
3541.5	285.4	0.6	0.62(5)	$M1/E2$	$12^- \to 11^-$	9
3541.5	557.4	2.5			$12^- \to 10^-$	9
3833.7	292.2		0.62(5)	$M1/E2$	$13^- \to 12^-$	9
3833.7	577.4				$13^- \to 11^-$	9
4142.9	309.4	2.5			$14^- \to 13^-$	9
4142.9	601.4	2.8			$14^- \to 12^-$	9

TABLE IV. *(Continued.)*

E_x (keV)	E_γ (keV)	$I_\gamma^{\text{rel.}}$	R	Multipolarity	$I^\pi_{\text{initial}} \rightarrow I^\pi_{\text{final}}$	Band
4461.1	317.7	2.9			$15^- \rightarrow 14^-$	9
4461.1	627.4	3.0			$15^- \rightarrow 13^-$	9
4787.4	325.8	2.0			$16^- \rightarrow 15^-$	9
4787.4	644.5	3.0			$16^- \rightarrow 14^-$	9
5089.5	302.4				$17^- \rightarrow 16^-$	9
5089.5	628.4				$17^- \rightarrow 15^-$	9
5089.5	1427.4				$17^- \rightarrow 16^+$	$9 \rightarrow 2$
5337.8	248.0	10.0	0.61(6)	$M1/E2$	$18^- \rightarrow 17^-$	9
5337.8	550.4	6.9			$18^- \rightarrow 16^-$	9
5531.7	718.6				$(20^-) \rightarrow 18^-$	Level $(20^-) \rightarrow 4$
5567.9	230.4		0.69(6)	$M1/E2$	$19^- \rightarrow 18^-$	9
5567.9	478.4				$19^- \rightarrow 17^-$	9
5811.2	243.2	0.62	0.56(7)	$M1/E2$	$20^- \rightarrow 19^-$	9
5811.2	473.4				$20^- \rightarrow 18^-$	9
5811.2	651.4				$20^- \rightarrow (18^-)$	$9 \rightarrow 7$
6081.5	262.1		0.60(6)	$M1/E2$	$21^- \rightarrow 20^-$	$9 \rightarrow 7$
6081.5	271.2		0.63(6)	$M1/E2$	$21^- \rightarrow 20^-$	9
6081.5	513.6	1.28			$21^- \rightarrow 19^-$	9
6372.4	290.6		0.62(5)	$M1/E2$	$22^- \rightarrow 21^-$	9
6372.4	552.5				$22^- \rightarrow 20^-$	$9 \rightarrow 7$
6372.4	561.2				$22^- \rightarrow 20^-$	9
6372.4	841.5				$22^- \rightarrow (20^-)$	$9 \rightarrow$ Level (20^-)
6685.0	313.1		0.60(5)	$M1/E2$	$23^- \rightarrow 22^-$	9
6685.0	603.5				$23^- \rightarrow 21^-$	9
7023.6	338.0	3.0			$24^- \rightarrow 23^-$	9
7023.6	651.2	1.18			$24^- \rightarrow 22^-$	9
7378.6	355.9	2.5	0.62(5)	$M1/E2$	$25^- \rightarrow 24^-$	9
7378.6	693.6	3.15			$25^- \rightarrow 23^-$	9
7761.2	382.0	2.37	0.67(6)	$M1/E2$	$26^- \rightarrow 25^-$	9
7761.2	737.6	3.35			$26^- \rightarrow 24^-$	9
8155.0	394.3	2.1	0.64(6)	$M1/E2$	$27^- \rightarrow 26^-$	9
8155.0	776.4	3.15			$27^- \rightarrow 25^-$	9
8570.0	413.8	2.35	0.70(6)	$M1/E2$	$28^- \rightarrow 27^-$	9
8570.0	808.8	1.6			$28^- \rightarrow 26^-$	9
8570.0	830.4				$28^- \rightarrow 26^-$	$9 \rightarrow 4$
9009.2	854.2	2.8			$29^- \rightarrow 27^-$	9
9009.2	440.4	2.8			$29^- \rightarrow 28^-$	9
9935.7	926.5				$(31^-) \rightarrow 29^-$	9
10920.7	985.0				$(33^-) \rightarrow (31^-)$	9
11884.6	963.9				$(35^-) \rightarrow (33^-)$	9
(12801.7)	(917.1)				$(37^-) \rightarrow (35^-)$	9
Band 10						
806.4					0^+	10
990.0	183.6				$2^+ \rightarrow 0^+$	10
1257.6	268.2				$4^+ \rightarrow 2^+$	10
1257.6	1065.4				$4^+ \rightarrow 2^+$	$10 \rightarrow 1$
1589.3	331.1	0.1			$(6^+) \rightarrow 4^+$	10
1589.2	404.8	0.4			$(6^+) \rightarrow (4^+)$	$10 \rightarrow 11$
1589.2	1062.4	1.0			$(6^+) \rightarrow 4^+$	$10 \rightarrow 1$
1589.2	618.6	2.0			$(6^+) \rightarrow 6^+$	$10 \rightarrow 1$
2018.6	429.4	1.0			$(8^+) \rightarrow (6^+)$	10
2018.6	1047.7	1.0			$(8^+) \rightarrow 6^+$	$10 \rightarrow 1$
2487.0	468.4	0.6			$(10^+) \rightarrow (8^+)$	10
2487.0	414.4	0.8			$(10^+) \rightarrow 10^+$	$10 \rightarrow 1$
Band 11						
820.3	820.3	0.2			$2^+ \rightarrow 0^+$	$11 \rightarrow 1$
820.3	628.5	0.2			$2^+ \rightarrow 2^+$	$11 \rightarrow 1$

TABLE IV. *(Continued.)*

E_x (keV)	E_γ (keV)	$I_\gamma^{\text{rel.}}$	R	Multipolarity	$I^\pi_{\text{initial}} \to I^\pi_{\text{final}}$	Band
1043.4	851.2	0.5			$3^+ \to 2^+$	$11 \to 1$
1184.4	363.7	0.2			$(4^+) \to 2^+$	11
1184.4	657.2	0.2			$(4^+) \to 4^+$	$11 \to 1$
1438.7	395.3	0.5			$5^+ \to 3^+$	11
1438.7	910.9	0.3			$5^+ \to 4^+$	$11 \to 1$
1913.0	474.3	0.3			$(7^+) \to 5^+$	11
1913.0	942.8	0.3			$(7^+) \to 6^+$	$11 \to 1$
2454.5	541.5	0.3			$(9^+) \to 7^+$	11
Band 12						
6718.2	1089.9	0.9			$(23^-) \to 22^+$	$12 \to 2$
7448.6	729.5	0.8			$(25^-) \to (23^-)$	12
7448.6	1014.8				$(25^-) \to 24^+$	$12 \to 2$
8242.1	792.3	0.5			$(27^-) \to (25^-)$	12
8242.1	962.9				$(27^-) \to 26^+$	$12 \to 2$
9099.5	856.3	0.5			$(29^-) \to (27^-)$	12
10014.9	915.7	0.3			$(31^-) \to (29^-)$	12
10971.3	955.7	0.2			$(33^-) \to (31^-)$	12
(11889.8)	(918.1)	0.1			$(35^-) \to (33^-)$	12
(12873.1)	(983.3)	0.1			$(37^-) \to (35^-)$	12
Band 13						
5567.4	755.1	1.0			$(20^-) \to 18^-$	$13 \to 4$
6297.4	730.0	0.8			$(22^-) \to (20^-)$	13
7097.0	799.6	0.6			$(24^-) \to (22^-)$	13
7954.3	857.3	0.5			$(26^-) \to (24^-)$	13
8868.3	914.0	0.3			$(28^-) \to (26^-)$	13
(9778.3)	(910.0)	0.1			$(30^-) \to (28^-)$	13

TABLE V. γ-ray energies E_γ (keV) and average transition quadrupole moments Q_t [31,32] for the TSD bands.

TSD band 1: $Q_t = 11.7^{+0.7}_{-0.8}$ eb E_γ (keV)	*TSD band 2:* $Q_t = 11.1^{+1.3}_{-1.0}$ eb E_γ (keV)	*TSD band 3:* $Q_t = 9.6^{+1.5}_{-1.1}$ eb E_γ (keV)
724.3	960.2	942.2
766.6	1007.4	986.3
802.3	1045.9	1035.1
841.7	1083.6	1083.7
875.0	1124.4	1133.0
901.5	1167.8	1182.4
932.6	1213.2	1231.5
972.7	1260.9	1281.8
1017.6	1309.2	1335.7
1064.3	1362.6	1393.5
1110.1	1419.7	1455.6
1156.3	1482.4	1515.4
1204.9		
1255.9		
1310.2		
1369.0		
1430.2		
1492.7		
1560.1		
1624.3		
1698.0		

[1] S. Cohen, F. Plasil, and W. J. Swiatecki, Ann. Phys. (NY) **82**, 557 (1974).

[2] A. Bohr and B. R. Mottelson, *Nuclear Structure*, Vol. II (W. A. Benjamin, New York, 1975).

[3] Z. Szymański, *Fast Nuclear Rotation* (Clarendon, Oxford, 1983).

[4] P. Ring and P. Schuck, *The Nuclear Many-Body Problem* (Springer-Verlag, Heidelberg, 1980).

[5] K. S. Krane, *Introductory Nuclear Physics* (John Wiley and Sons, New York, 1988).

[6] H. Ejiri and M. J. de Voigt, *Gamma-Ray and Electron Spectroscopy in Nuclear Physics* (Clarendon, Oxford, 1989).

[7] S. G. Nilsson and I. Ragnarsson, *Shapes and Shells in Nuclear Structure* (Cambridge University Press, Cambridge, UK, 1995).

[8] K. Heyde, *Basic Ideas and Concepts in Nuclear Physics* (Institute of Physics, Bristol, 1999).

[9] R. F. Casten, *Nuclear Structure from a Simple Perspective*, 2nd ed. Oxford Studies in Nuclear Physics (Oxford University Press, 2001).

[10] S. C. Pancholi, *Exotic Nuclear Excitations*, Springer Tracts in Modern Physics (Springer-Verlag, Berlin, 2011).

[11] X. Wang, M. A. Riley, E. S. Paul, and J. Simpson, *McGraw-Hill Yearbook of Science and Technology* (McGraw-Hill, New York, 2013).

[12] M. A. Riley, J. Simpson, and E. S. Paul, Phys. Scr. **91**, 123002 (2016).

[13] B. G. Carlsson and I. Ragnarsson, Phys. Rev. C **74**, 011302(R) (2006).

[14] K. Pomorski and J. Dudek, Phys. Rev. C **67**, 044316 (2003).

[15] E. S. Paul, P. J. Twin, A. O. Evans, A. Pipidis, M. A. Riley, J. Simpson, D. E. Appelbe, D. B. Campbell, P. T. W. Choy, R. M. Clark, M. Cromaz, P. Fallon, A. Görgen, D. T. Joss, I. Y. Lee, A. O. Macchiavelli, P. J. Nolan, D. Ward, and I. Ragnarsson, Phys. Rev. Lett. **98**, 012501 (2007).

[16] A. Johnson, H. Ryde, and J. Sztarkier, Phys. Lett. B **34**, 605 (1971).

[17] R. Wyss and M. A. Riley, Nucl. Phys. News **32**, 16 (2022).

[18] I. Y. Lee, M. M. Aleonard, M. A. Deleplanque, Y. El-Masri, J. O. Newton, R. S. Simon, R. M. Diamond, and F. S. Stephens, Phys. Rev. Lett. **38**, 1454 (1977).

[19] J. Burde, E. L. Dines, S. Shih, R. M. Diamond, J. E. Draper, K. H. Lindenberger, C. Schück, and F. S. Stephens, Phys. Rev. Lett. **48**, 530 (1982).

[20] J. Simpson, M. A. Riley, J. R. Cresswell, P. D. Forsyth, D. Howe, B. M. Nyakó, J. F. Sharpey-Schafer, J. Bacelar, J. D. Garrett, G. B. Hagemann, B. Herskind, and A. Holm, Phys. Rev. Lett. **53**, 648 (1984).

[21] P. O. Tjøm, R. M. Diamond, J. C. Bacelar, E. M. Beck, M. A. Deleplanque, J. E. Draper, and F. S. Stephens, Phys. Rev. Lett. **55**, 2405 (1985).

[22] E. M. Beck, H. Hubel, R. M. Diamond, J. C. Bacelar, M. A. Deleplanque, K. H. Maier, R. J. McDonald, and F. S. Stephens, and P. O. Tjøm, Phys. Lett. B **215**, 624 (1988).

[23] J. Simpson, M. A. Riley, S. J. Gale, J. F. Sharpey-Schafer, M. A. Bentley, A. M. Bruce, R. Chapman, R. M. Clark, S. Clarke, J. Copnell, D. M. Cullen, P. Fallon, A. Fitzpatrick, P. D. Forsyth, S. J. Freeman, P. M. Jones, M. J. Joyce, F. Liden, J. C. Lisle, A. O. Macchiavelli A. G. Smith, J. F. Smith, J. Sweeney, D. M. Thompson, S. Warburton, J. N. Wilson, T. Bengtsson, and I. Ragnarsson, Phys. Lett. B **327**, 187 (1994).

[24] M. A. Riley, M. K. Djongolov, A. O. Evans, D. J. Hartley, R. V. F. Janssens, E. S. Paul, J. Simpson, A. A. Aguilar, D. E. Appelbe, C. R. Bingham, D. B. Campbell, M. P. Carpenter, P. Chowdhury, P. T. W. Choy, R. M. Clark, M. Cromaz, D. M. Cullen, M. Danchev, G. D. Dracoulis, P. Fallon *et al.*, Phys. Scr. **T125**, 123 (2006).

[25] T. Bengtsson and I. Ragnarsson, Phys. Scr. **T5**, 165 (1983).

[26] J. Dudek and W. Nazarewicz, Phys. Rev. C **31**, 298 (1985).

[27] I. Ragnarsson, Z. Xing, T. Bengtsson, and M. A. Riley, Phys. Scr. **34**, 651 (1986).

[28] A. O. Evans, E. S. Paul, J. Simpson, M. A. Riley, D. E. Appelbe, D. B. Campbell, P. T. W. Choy, R. M. Clark, M. Cromaz, P. Fallon, A. Görgen, D. T. Joss, I. Y. Lee, A. O. Macchiavelli, P. J. Nolan, A. Pipidis, D. Ward, I. Ragnarsson, and F. Saric, Phys. Rev. Lett. **92**, 252502 (2004).

[29] A. O. Evans, E. S. Paul, J. Simpson, M. A. Riley, D. E. Appelbe, D. B. Campbell, P. T. W. Choy, R. M. Clark, M. Cromaz, P. Fallon, A. Gorgen, D. T. Joss, I. Y. Lee, A. O. Macchiavelli, P. J. Nolan, A. Pipidis, D. Ward, and I. Ragnarsson, Phys. Rev. C **73**, 064303 (2006).

[30] A. Pipidis, Ph.D. thesis, Florida State University, 2006 (unpublished), http://purl.flvc.org/fsu/fd/FSU_migr_etd-0687.

[31] X. Wang, M. A. Riley, J. Simpson, E. S. Paul, J. Ollier, R. V. F. Janssens, A. D. Ayangeakaa, H. C. Boston, M. P. Carpenter, C. J. Chiara, U. Garg, D. J. Hartley, D. S. Judson, F. G. Kondev, T. Lauritsen, N. M. Lumley, J. Matta, P. J. Nolan, M. Petri, J. P. Revill *et al.*, Phys. Lett. B **702**, 127 (2011).

[32] X. Wang, M. A. Riley, J. Simpson, E. S. Paul, R. V. F. Janssens, A. D. Ayangeakaa, H. C. Boston, M. P. Carpenter, C. J. Chiara, U. Garg, P. Hampson, D. J. Hartley, C. R. Hoffman, D. S. Judson, F. G. Kondev, T. Lauritsen, N. M. Lumley, J. Matta, S. Miller, P. J. Nolan *et al.*, J. Phys.: Conf. Ser. **381**, 012065 (2012).

[33] I. Y. Lee, Nucl. Phys. A **520**, c641 (1990).

[34] R. V. F. Janssens and F. S. Stephens, Nucl. Phys. News **6**, 9 (1996).

[35] M. Cromaz, T. J. M. Symons, G. J. Lane, I. Y. Lee, and R. W. MacLeod, Nucl. Instrum. Methods Phys. Res., Sect. A **462**, 519 (2001).

[36] D. C. Radford, Nucl. Instrum. Methods Phys. Res., Sect. A **361**, 306 (1995).

[37] D. C. Radford, M. Cromaz, and C. J. Beyer, in *Proceedings of the Nuclear Structure 98 Conference*, Gatlinburg, 1998, edited by C. Baktash, AIP Conf. Proc. No. 481 (AIP, New York, 1999), pp. 570–580.

[38] K. Krane, R. Steffen, and R. Wheeler, At. Data Nucl. Data Tables **11**, 351 (1973).

[39] R. Steffen and K. Alder, *The Electromagnetic Interaction in Nuclear Spectroscopy* (Noth-Holland, Amsterdam, 1975).

[40] L. P. Ekström and A. Nordlund, Nucl. Instrum. Methods Phys. Res., Sect. A **313**, 421 (1992).

[41] E. S. Paul, S. V. Rigby, M. A. Riley, J. Simpson, D. E. Appelbe, D. B. Campbell, P. T. W. Choy, R. M. Clark, M. Cromaz, A. O. Evans, P. Fallon, A. Görgen, D. T. Joss, I. Y. Lee, A. O. Macchiavelli, P. J. Nolan, A. Pipidis, D. Ward, and I. Ragnarsson, Phys. Rev. C **79**, 044324 (2009).

[42] M. A. Riley, Ph.D. thesis, University of Liverpool, 1984 (unpublished).

[43] J. Simpson, P. A. Butler, P. D. Forsyth, J. F. Sharpey-Schafer, J. D. Garrett, G. B. Hagemann, B. Herskind, and L. P. Ekström, J. Phys. G **10**, 383 (1984).

[44] T. Yamazaki, Nucl. Data **3**, 1 (1967).

[45] E. Der Mateosian and A. W. Sunyar, At. Data Nucl. Data Tables **13**, 391 (1974).

[46] P. Aguer, C. F. Liang, J. Libert, P. Paris, A. Peghaire, A. Charvet, R. Duffait and G. Marguier, Nucl. Phys. A **249**, 239 (1975).

[47] T. R. S. Dinoko *et al.* (unpublished); T. R. S. Dinoko, Ph.D. thesis, University of Western Cape, South Africa, 2013 (unpublished), https://etd.uwc.ac.za/handle/11394/3245.

[48] R. Bengtsson and S. Frauendorf, Nucl. Phys. A **314**, 27 (1979).

[49] R. Bengtsson and S. Frauendorf, Nucl. Phys. A **327**, 139 (1979).

[50] R. Bengtsson, S. Frauendorf, and F.-R. May, At. Data Nucl. Data Tables **35**, 15 (1986).

[51] M. A. Riley, J. Simpson, R. Aryaeinejad, J. R. Cresswell, P. D. Forsyth, D. Howe, P. J. Nolan, B. M. Nyakó, J. F. Sharpey-Schafer, P. J. Twin, J. Bacelar, J. D. Garrett, G. B. Hagemann, B. Herskind, and A. Holm, Phys. Lett. B **135**, 275 (1984).

[52] L. L. Riedinger, O. Andersen, S. Frauendorf, J. D. Garrett, J. J. Gaardhøje, G. B. Hagemann, B. Herskind, Y. V. Makovetzky, J. C. Waddington, M. Guttormsen, and P. O. Tjøm, Phys. Rev. Lett. **44**, 568 (1980).

[53] S. M. Harris, Phys. Rev. **138**, B509 (1965).

[54] J. Simpson, P. D. Forsyth, D. Howe, B. M. Nyakó, M. A. Riley, J. F. Sharpey-Schafer, J. Bacelar, J. D. Garrett, G. B. Hagemann, B. Herskind, and A. Holm, and P. O. Tjøm, Phys. Rev. Lett. **54**, 1132 (1985).

[55] D. C. Radford, H. R. Andrews, G. C. Ball, D. Horn, D. Ward, F. Banville, S. Flibotte, S. Monaro, S. Pilotte, P. Taras, J. K. Johansson, D. Tucker, J. C. Waddington, M. A. Riley, G. B. Hagemann, and I. Hamamoto, Nucl. Phys. A **545**, 665 (1992).

[56] S. Jonsson, N. Roy, H. Ryde, W. Walus, J. Kownacki, J. D. Garrett, G. B. Hagemann, B. Herskind, R. Bengtsson, and S. Aberg, Nucl. Phys. A **449**, 537 (1986).

[57] J. N. Mo, S. Sergirva, R. Chapman, J. C. Lisle, E. Paul, J. C. Willmott, J. Hattula, M. Jääskeläinen, J. Simpson, P. M. Walker, J. D. Garrett, G. B. Hagemann, B. Herskind, M. A. Riley, and G. Sletten, Nucl. Phys. A **472**, 295 (1987)

[58] J. Simpson, M. A. Riley, J. R. Cresswell, D. V. Elenkov, P. D. Forsyth, G. B. Hagemann, D. Howe, B. M. Nyako, S. Ogaza, J. C. Lisle, and J. F. Sharpey-Schafer, J. Phys. G: Nucl. Phys. **13**, 847 (1987).

[59] M. A. Riley, J. Simpson, J. F. Sharpey-Schafer, J. R. Cresswell, H. W. Cranmer-Gordon, P. D. Forsyth, D. Howe, A. H. Nelson, P. J. Nolan, P. J. Smith, N. J. Ward, J. C. Lisle, and P. M. Walker, Nucl. Phys. A **486**, 456 (1988).

[60] J. D. Garrett, G. B. Hagemann, B. Herskind, J. Bacelar, R. Chapman, J. C. Lisle, J. N. Mo, A. Simcock, J. C. Willmott, and H. G. Price, Phys. Lett. B **118**, 297 (1982).

[61] J. Simpson, M. A. Riley, R. W. Laird, D. J. Hartley, F. G. Kondev, J. Sweeney, A. N. Wilson, S. J. Gale, M. A. Bentley, A. M. Bruce, R. Chapman, R. M. Clark, D. M. Cullen, P. Fallon, P. D. Gorsyth, S. J. Freeman, P. M. Jones, J. C. Lisle, A. O. Macchiavelli, J. F. Sharpey-Schafer, A. G. Smith, J. F. Smith, and D. M. Thompson, Eur. Phys. J. A **1**, 267 (1998).

[62] J. R. B. Oliveira, S. Frauendorf, M. A. Deleplanque, B. Cederwall, R. M. Diamond, A. O. Macchiavelli, F. S. Stephens, J. Burde, J. E. Draper, C. Duyar, E. Rubel, J. A. Becker, E. A. Henry, M. J. Brinkman, A. Kuhnert, M. A. Stoyer, and T. F. Wang, Phys. Rev. C **50**, 1360 (1994).

[63] S. J. Gale, J. Simpson, M. A. Riley, J. F. Sharpey-Schafer, M. A. Bentley, A. M. Bruce, R. Chapman, R. M. Clark, S. Clarke, J. Copnell, D. M. Cullen, P. Fallon, A. Fitzpatrick, P. D. Forsyth, S. J. Freeman, P. M. Jones, M. J. Joyce, F. Liden, J. C. Lisle, A. O. Macchiavelli, A. G. Smith, J. F. Smith, J. Sweeney, D. M. Thompson, S. Warburton, J. N. Wilson, and I. Ragnarsson, J. Phys. G Nucl. Part. Phys. **21**, 193 (1995).

[64] M. A. Deleplanque, J. C. Bacelar, E. M. Beck, R. M. Diamond, J E. Draper, R. J. McDonald, and F. S. Stephens, Phys. Lett. B **193**, 422 (1987).

[65] M. Mustafa, J. Ollier, J. Simpson, M. A. Riley, E. S. Paul, X. Wang, A. Aguilar, M. P. Carpenter, I. G. Darby, D. J. Hartley, R. V. F. Janssens, F. G. Kondev, T. Lauritsen, P. J. Nolan, M. Petri, J. M. Rees, J. P. Revill, S. V. Rigby, C. Teal, J. Thomson *et al.*, Phys. Rev. C **84**, 054320 (2011).

[66] F. Dönau and S. Frauendorf, in *Proceedings of the Conference on High Angular Momentum Properties of Nuclei*, Oak Ridge, 1982, edited by N. R. Johnson (Harwood Academic, New York, 1983), p. 143.

[67] F. Dönau, Nucl. Phys. A **471**, 469 (1987).

[68] S. G. Nilsson, Dan. Mat. Fys. Medd. **29**, 1 (1955).

[69] R. A. Bark, P. Bosetti, G. B. Hagemann, H. Ryde, A. Brockstedt, H. Carlsson, L. P. Ekström, A. Nordlund, B. Herskind, S. Leoni, A. Bracco, F. Camera, S. Frattini, M. Mattiuzzi, B. Million, C. Rossi-Alvarez, G. de Angelis, D. Bazzacco, S. Lunardi, and M. De Poli, Z. Phys. A **359**, 5 (1997).

[70] T. Bengtsson, Nucl. Phys. A **512**, 124 (1990).

[71] A. Pipidis, M. A. Riley, J. Simpson, R. V. F. Janssens, F. G. Kondev, D. E. Appelbe, A. P. Bagshaw, M. A. Bentley, T. B. Brown, M. P. Carpenter, D. M. Cullen, D. B. Campbell, P. J. Dagnall, P. Fallon, S. M. Fischer, G. B. Hagemann, D. J. Hartley, K. Lagergren, R. W. Laird, T. Lauritsen *et al.*, Phys. Rev. C **72**, 064307 (2005).

[72] P. J. Twin, B. M. Nyako, A. H. Nelson, J. Simpson, M. A. Bentley, H. W. Cranmer-Gordon, P. D. Forsyth, D. Howe, A. R. Mokhtar, J. D. Morrison, J. F. Sharpey-Schafer, and G. Sletten, Phys. Rev. Lett. **57**, 811 (1986).

[73] T. Lauritsen, M. P. Carpenter, T. Dossing, P. Fallon, B. Herskind, R. V. F. Janssens, D. G. Jenkins, T. L. Khoo, F. G. Kondev, A. Lopez-Martens, A. O. Macchiavelli, D. Ward, K. S. Abu Saleem, I. Ahmad, R. Clark, M. Cromaz, J. P. Greene, F. Hannachi, A. M. Heinz, A. Korichi, G. Lane, C. J. Lister, P. Reiter, D. Seweryniak, S. Siem, R. C. Vondrasek, and I. Wiedenhover, Phys. Rev. Lett. **88**, 042501 (2002).

[74] S. W. Ødegård, G. B. Hagemann, D. R. Jensen, M. Bergström, B. Herskind, G. Sletten, S. Törmänen, J. N. Wilson, P. O. Tjøm, I. Hamamoto, K. Spohr, H. Hübel, A. Görgen, G. Schönwasser, A. Bracco, S. Leoni, A. Maj, C. M. Petrache, P. Bednarczyk, and D. Curien, Phys. Rev. Lett. **86**, 5866 (2001).

[75] D. R. Jensen, G. B. Hagemann, I. Hamamoto, S. W. Ødegård, M. Bergström, B. Herskind, G. Sletten, S. Törmänen, J. N. Wilson, P. O. Tjøm, K. Spohr, H. Hübel, A. Görgen, G. Schönwasser, A. Bracco, S. Leoni, A. Maj, C. M. Petrache, P. Bednarczyk, and D. Curien, Nucl. Phys. A **703**, 3 (2002).

[76] J. Ollier, J. Simpson, X. Wang, M. A. Riley, A. Aguilar, C. Teal, E. S. Paul, P. J. Nolan, M. Petri, S. V. Rigby, J. Thomson, C. Unsworth, M. P. Carpenter, R. V. F. Janssens, F. G. Kondev, T. Lauritsen, S. Zhu, D. J. Hartley, I. G. Darby, and I. Ragnarsson, Phys. Rev. C **80**, 064322 (2009).

[77] J. F. Sharpey-Schafer, S. M. Mullins, R. A. Bark, J. Kau, F. Komati, E. A. Lawrie, T. E. Madiba, P. Maine, A. Minkova, S. H. T. Murry, N. J. Ncapayi, and P. A. Vymers, Eur. Phys. J. A **47**, 5 (2011).

[78] J. M. Rees, E. S. Paul, M. A. Riley, J. Simpson, A. D. Ayangeakaa, H. C. Boston, M. P. Carpenter, C. J. Chiara, U. Garg, D. J. Hartley, R. V. F. Janssens, D. S. Judson, F. G. Kondev, T. Lauritsen, N. M. Lumley, J. Matta, P. J. Nolan, J. Ollier, M. Petri, J. P. Revill *et al.*, Phys. Rev. C **83**, 044314 (2011).

[79] J. F. Sharpey-Schafer, R. A. Bark, S. P. Bvumbi, T. R. S. Dinoko, and S. N. T. Majola, Eur. Phys. J. A **55**, 15 (2019).

[80] I. Ragnarsson and R. A. Broglia, Nucl. Phys. A **263**, 315 (1976).

[81] J. M. Rees, E. S. Paul, J. Simpson, M. A. Riley, A. D. Ayangeakaa, M. P. Carpenter, C. J. Chiara, U. Garg, P. Hampson, D. J. Hartley, C. R. Hoffman, R. V. F. Janssens, F. G. Kondev, T. Lauritsen, P. J. R. Mason, J. Matta, S. L. Miller, P. J. Nolan, J. Ollier, M. Petri, D. C. Radford, J. P. Revill, X. Wang, S. Zhu, J. Gellanki, and I. Ragnarsson, Phys. Rev. C **91**, 054301 (2015).

[82] E. S. Paul, J. M. Rees, P. Hampson, M. A. Riley, J. Simpson, A. D. Ayangeakaa, J. S. Baron, M. P. Carpenter, C. J. Chiara, U. Garg, D. J. Hartley, C. R. Hoffman, R. V. F. Janssens, F. G. Kondev, T. Lauritsen, P. J. R. Mason, J. Matta, S. L. Miller, P. J. Nolan, J. Ollier *et al.*, Acta Phys. Pol. B **46**, 487 (2015).

[83] Y. Shi, J. Dobaczewski, S. Frauendorf, W. Nazarewicz, J. C. Pei, F. R. Xu, and N. Nikolov, Phys. Rev. Lett. **108**, 092501 (2012).

[84] Y. Shi, C. L. Zhang, J. Dobaczewski, and W. Nazarewicz, Phys. Rev. C **88**, 034311 (2013).

[85] A. Kardan, I. Ragnarsson, H. Miri-Hakimabad, and L. Rafat-Motevali, Phys. Rev. C **86**, 014309 (2012).

[86] A. V. Afanasjev, Y. Shi, and W. Nazarewicz, Phys. Rev. C **86**, 031304(R) (2012).

[87] I. Ragnarsson, Phys. Scr. **92**, 124004 (2017).

[88] I. Y. Lee, M. A. Deleplanque, and K. Vetter, Rep. Prog. Phys. **66**, 1095 (2003).

[89] W. Korten *et al.*, Eur. Phys. J. A **56**, 137 (2020).